AN ABSTRACT FOR THE THESIS OF

Jacqueline K. Garcia for the degree of Master of Science in Radiation Health Physics presented on June 18, 2020.

Title: Creating Anthropomorphic Models with Mesh Phantoms in MCNP to Simulate Mammography

Abstract approved: _____

Steven R. Reese

Breast cancer is the most common cancer among women as it accounts for about 25% of all female cancer cases. Studies have shown that early detection of breast cancer increases the chances of a positive prognosis amongst patients therefore it is crucial to provide accurate diagnosis tools in routine exams. Experimenting with new techniques and tools that can provide increased accuracy requires time-consuming and costly studies, therefore, simulating outcomes that have high potential can provide guidance for increased accuracy without requiring expensive tests. This project outlines the possibility of developing an advanced anthropomorphic mesh phantom of the breast to experiment different contrast agents with. The phantom would contain all the components of a real breast and it would be able to simulate the physiological and metabolic components that play a role in the outcome of a real tomosynthesis-mammography scan. This project focuses on creating a basic model of a breast and a tomosynthesis system that provides an indication on whether a simulation system can be produced. The materials used for this project include Abaqus/CAE software, Python, MCNP6.2, and scripting tools as well as resources on tomosynthesis equipment. The results demonstrated a positive outcome thus indicating that the model can be further developed to incorporate the multiple components of a real breast scan to increase the simulation's realism. Further work on this project will focus on increasing the model's complexity and incorporating contrast agents so that the efficacy of each can be explored.

Creating Anthropomorphic Models with Mesh Phantoms in MCNP
to Simulate Mammography

by
Jacqueline K. Garcia

A THESIS

Submitted to

Oregon State University

in partial fulfillment of
the requirements for the
degree of

Master of Science

Presented June 18, 2020
Commencement June 2021

Master of Science thesis of Jacqueline K. Garcia presented on June 18, 2020.

APPROVED:

_____

Major Professor, representing Radiation Health Physics

_____

Head of the School of Nuclear Science and Engineering

_____

Dean of the Graduate School

I understand that my thesis will become part of the permanent collection of Oregon State University libraries. My signature below authorizes release of my thesis to any reader upon request.

_____

Jacqueline K. Garcia, Author

ACKNOWLEDGEMENTS

I would like to thank the department of Nuclear Science and Engineering at Oregon State University for providing me with the opportunity to study, preform research, and grow.

I would like to thank my advisor, Dr. Steven Reese, for providing me with the opportunity to work on this project and for providing ideas while I was still trying to find my footing in this program. Thank you for being patient, understanding, and believing in me.

I would also like to thank the professors at the department of Nuclear Science and Engineering for providing engaging lectures and for inspiring me so that I may one day contribute to the field. I'd like to thank my committee, Camille Palmer, Lily Ranjbar, Salam Alhawsawsi, Russ Turner, and again, my advisor Steven Reese, for setting aside time for me and this project.

A special thank you to all the friends I met at Oregon State; you motivated me to do my best and provided me with happiness in the bleakest of times. I'd also like to thank my friends from UC Berkeley who stayed in contact with me and continuously showed an interest in my wellbeing: Jason Coffman, Maaz Siddiqui, A.J. Albaaj, Chris Lamb, and Ava Shahi. I'd like to thank my sister, Martha Garcia, for always believing in me and for providing support when I needed it most.

A very special thank you to Bill Gates for funding my education, and that of several other scholars, as a 10-year commitment so that I would never have to worry about educational expenses.

Finally, thank you to all the women in STEM for marching forward and breaking barriers to make it easier for future generations to live in a world with gender equality.

TABLE OF CONTENTS

LIST OF FIGURES

LIST OF TABLES

1 Introduction

Breast cancer is a large contributor to mortality among women of older age and while most breast cancer cases don't lead to death, its impact can still be devastating, especially if not diagnosed early. This project seeks to propose a solution, or at least an aid, to a key issue that underlies breast cancer mortality, which is inadequate imaging of breast tumors and lack of tumor identification among women with dense breasts. By exploring tools and techniques that can facilitate breast imaging and improve the identification of tumors during routine examination, the survival rate of women with breast cancer, especially those with dense breasts, increases. The basis of this project is to create the option of exploring the efficacy of a contrast agent before time and money is invested into exploratory studies that may not be fruitful. Developing a tool that simulates the performance of multiple contrast agents in a realistic breast phantom provides indication if the contrast agent is worth investing in. By exploring the impact of the contrast agent's effective Z, half-life, and several of its physical properties, on a realistic breast model, multiple contrast agents that show promise in the simulations can be proposed. In addition, the limitations and the relationship between contrast agent and breast properties can be explored; a contrast agent might be compatible with a fatty breast but not as compatible with a dense breast. This information is important and plays a vital role in the future of contrast agents in breast cancer detection.

Creating a realistic phantom model of a breast is not easy. There are several components present in breast anatomy and many of those influence the outcome of a mammography screening. For example, high stroma content increases the density and decreases tumor visibility. In addition, the physiological components also need to be considered, such as blood flow and vessel density, since these components determine the distribution and half-life of the contrast agent inside the breast. Because incorporating the complexity and accuracy of breast components into a breast phantom is challenging and time consuming, the project is broken up into two main stages. The first stage is a trial stage that ensures the simulation works. This means the mesh phantom is capable of being imaged by simulated tomosynthesis equipment and a reliable radiograph is produced. The second stage incorporates the realistic features in a breast model and incorporates the correct mechanics behind an accurate tomosynthesis system, including the sources of

noise and the sensitivity of the system. This is also the stage that incorporates the contrast agents into the breast model to examine their efficacy. This paper is based on the first stage project. The results for this stage are very important because they provide an indication for the feasibility of the overarching project. If the results for the initial stage are poor, then the second stage cannot work.

This paper will discuss the multiple aspects to this project and more specifically, the development and results of the first stage. Since the first stage's purpose is to ensure the second stage is feasible, a complicated breast model is not needed. Therefore, the model is given a simple geometry: a compressed sphere that takes on the shape of a truncated semi-cylinder, and the tumor is the shape of a small sphere. The model is constructed with the Abaqus meshing tool using Python scripting written in Atom.io. Atom.io is also used to write the MCNP input file, which contains the information to create the tomosynthesis simulation. The Abaqus mesh model of the breast is 'called' into the MCNP input script and communication is established between the two programs. The source is created based on MCNP's Fortran code and the source is also rotated across 15 projections to mimic the moving of a tomosynthesis x-ray source. The detector component is created with a mesh tally and the results are plotted with Python plotting tools. This paper outlines the background information, the procedure, and the results of this project.

1.1 Motivation

Breast cancer is widespread; it is a disease that causes anxiety and ambiguity in the lives of victims. It strikes randomly and when routine examinations are done, it is impossible to predict whether the patient is affected until after the results are provided. Therefore, each routine examination needs to be thorough and accurate. The ambiguity of radiography results increases with breast density and while mammography systems have a relatively good sensitivity for women with less-dense breasts, women with dense breasts experience a significant reduction in sensitivity. In addition, women with dense breasts are more predisposed to developing breast cancer. Therefore, tools need to be developed to increase the efficacy of breast cancer diagnostic equipment.

Contrast agents have already been proposed as a solution to increase tumor visibility during routine scans, however, the efficacy of these iodine-based contrast agents can be improved. There are several other contrast agents that have been proposed for use in medical imaging, such as those with a higher density or those with more attenuating particles, such as gold and bismuth. However, whether they work better than iodine is unknown, or not explored in detail. Therefore, the motivation behind this project is the need to explore the efficacy of contrast agents using rudimentary physics instead of costly and time-consuming studies that are often lacking in patients. A good study needs to encapsulate the variety of breast cancer patients: from variability in breast density to variability in tumor type, size, and location. This is hard to accomplish because studies involving breast cancer patients are often small: about 50 patients, therefore, the connection between tumor visibility and the multiple variables involved in breast cancer is difficult to establish. This project will provide insight into the relationship between tumor visibility, contrast agents, and breast cancer variability. By creating this relationship, contrast agents that work for dense breasts by increasing tumor visibility can be proposed.

1.2 Objectives

This first stage project aims at proving that a tomosynthesis simulation can be preformed on a mesh anthropomorphic model of a breast. This can be broken down into multiple components:

- Proving that a rotating source that simulates tomosynthesis can be created. This is a basic requirement for the modeled system since a rotating source is a staple of a tomosynthesis imaging system.

- Proving that an Abaqus model can be created and 'called' into MCNP by incorporating the Abaqus input file name into the MCNP input file. If MCNP recognizes the Abaqus model, then no error will be produced and the embedded mesh can be seen in the MCNP output file.

- Proving that the tumor can be differentiated in MCNP if given enough contrast agent. If the embedded tumor is given an iodine-containing material, then the tumor should be distinguishable from the breast tissue in the radiograph.

- The radiograph demonstrates the clear shape of the breast and the embedded tumor. By demonstrating that the breast and tumor shapes are un-warped and free of distortion, the results demonstrate that MCNP's mesh tally tool can produce accurate radiographs.

If all these objectives are completed with positive results, then the first stage of the project provides enough evidence to further advance the model so that a more accurate tomosynthesis simulation can be conducted in the second stage.

2 Background and Literature Review

To fully understand the basis for this project, some background information is needed. The key terms provided in the following section are common in the imaging field and will come up frequently throughout this paper. The **Related Work** section provides information on similar projects to this one and provides helpful details that help create the scope of this project. The literature review provided in this paper is meant to guide the reader through the several components of this project and allows the reader to learn about the importance of each component.

2. 1 Key Terms

Mammography: A process that uses low-energy x-rays (ranging from about 20-40 keV) to screen human breasts for signs of tumors. A mammography can be performed to obtain a screening mammogram or a diagnostic mammogram. A diagnostic mammogram's purpose is to further investigate a confirmed growth that was seen in a screening mammogram.

Digital Mammography: This form of mammography uses x-rays as well, however, instead of utilizing x-ray film to capture the resulting image, digital receptors and computers are used for image processing. This allows for image manipulation thus allowing radiologists to better distinguish between different masses.[1]

Breast Density Scale (BDS): The breast density scale was determined from Breast Imaging Reporting and Data System (BI-RADS) and contains 4 types of breast densities[2,3]:

- Type A (1): lowest density with breast composition consisting of mostly fat with less than 25% of the breast consisting of fibroglandular tissue.

- Type B (2); second lowest density of breast with a fibroglandular tissue composition of about 30-40%. The primary tissue is still fatty tissue and the fibroglandular areas are scattered.

- Type C (3): the fibroglandular tissue and fatty tissue are 'homogeneously' distributed with a fibroglandular composition of up to 60%. At this density, small masses might be obscured

- Type D (4): extremely dense breast composed primarily of fibroglandular tissue (almost entirely) which lowers mammography sensitivity.

Contrast Agents: Contrast agents (often presented through an injection) contain molecules that can enhance imaging by providing supplemental contrast between the target tissue and the surrounding tissue. Iodine is commonly used in contrast agents used in mammography and computer tomography. A good contrast agent should have a high affinity for the target tissue and a low affinity for the surrounding tissue.

Computed Tomography (CT): this imaging technique utilizes computer-processed x-ray measurements taken at multiple angles to create 'slices' of internal structural components of the body. The contrast shown in CT images is caused by the difference in x-ray absorption among the different tissues irradiated.[4]

Tomosynthesis: high-resolution tomography is similar to computer tomography including reconstruction algorithms used and x-ray energy, however, tomosynthesis uses a limited rotation angle of about 15-60 degrees thus producing images with a limited depth of field. However, different depths and thicknesses can be reconstructed with the use of image processing techniques.[5]

Magnetic Resonance Imaging (MRI): MRI does not use ionizing radiation, but instead, magnetic fields to generate images of structural or metabolic processes inside the body. This form of imaging has a high sensitivity and high resolution.

Monte Carlo Particle Transport Code (MCNP): This is a program used to generate and track (essentially simulating) multiple different types of particles over a broad range of energy and conditions. This program replaces expensive and often impossible experiments by providing accurate simulations of nuclear transport scenarios.

Image Simulation: Medical imaging simulations can be performed using MCNP and resulting images can be generated using the following reduction techniques: rastering, point detectors, and component separation.[6]

2.2 Related Work

Monte Carlo simulations have been used in radiological sciences to explore radioparticle interactions within the human body. Although there has been no previous work done that explores the versatility of contrast agents for breast screening purposes using Monte Carlo simulations, there has been research conducted that utilizes MCNP to construct simulated x-ray beams, human phantoms, and image reconstruction. Several of the research projects that have performed similar simulations using MCNP have done so for the purpose of simulating dose absorption during radiological imaging.

In order to simulate radioparticle interactions within humans, researchers often create phantom models of the target organ(s) or tissue(s) they are trying to explore. In a paper titled *Breast Dosimetry Using High-Resolution Voxel Phantoms*, Dance[7] created a Monte Carlo model to simulate particle (x-ray) interactions within a breast for dose calculations. The dose was calculated at various points in the breast to determine a conversion factor, 'g,' empirically as a function of distance from the glandular region. In this model, the photons emerged from a focal spot which was defined as the x-ray tube. The model followed the photons as they emerged from the x-ray tube, into the compression plate, then into the tissue where they followed a series of interactions, including scattering and absorption. The results of these interactions were then recorded to calculate an approximation of dose deposited in each tissue. The breast voxel phantoms used were generalized and placed the glandular tissue (composing 69% of the total mass) in the central

region instead of following the distribution of glandularity in Type C and Type D breasts. In addition, the voxel phantoms were used for 2D simulation instead of 3D simulations, thus gravely reducing the accuracy of the model.

In a different project, dose to the breast was approximated using calculations of dose to the target tissue, glandular tissue, using GEANT4 with the Monte Carlo method. In the paper, *Internal breast dosimetry in mammography: Monte Carlo validation in homogeneous and anthropomorphic breast phantoms with a clinical mammography system*, Fedon and Caballo[8] created both computer-simulated breast phantoms as well as anthropomorphic breast phantoms to compare computer-calculated dose versus physically calculated dose. The physical model utilized TLDs (thermoluminescent dosimeters) to calculate the dose imparted upon the anthropomorphic model while the computer model used Monte Carlo simulations. In this project, the computer-generated breast phantoms were created with both homogeneous and heterogeneous compositions (two separate models). However, the computer model also used 2D projections while the anthropomorphic model was 3D. The results showed agreement between both the computer models and the anthropomorphic model; the models demonstrated similar dose deposition in the breast tissue.

Both projects described used voxel phantoms to calculate dose imparted to the tissue and therefore do not provide detail on mammographic images resulting from the mammography simulation. Related work on Monte Carlo breast imaging simulations is described in a paper titled *Monte Carlo Modeling of Mammographic Image* by Peplow and Verghese[9]. In this project, breast cancer calcifications were simulated and imaged using MCNP. The results were then compared with a digital image of a mammography conducted at 32 keV. The results demonstrated great accuracy between the MCNP-generated image of the calcification and the real image.

There are several other examples that have used phantoms to replace real human tissue for the purpose of Monte Carlo simulations, but few utilize an accurate model to describe all four different breast densities and varying glandular distribution. In order to create an accurate model for this project, the tissue (both adipose and glandular) distribution must be considered as well as the vascularization, which plays an

important role in breast cancer. A very fine model (sub-centimeter resolution) is therefore essential because unlike the dose calculation simulations, which primarily depend on the mass composition, this model depends on the spatial distribution of the tissue and vasculature because this will impact the visibility of the breast tumors.

2.3 Review of Literature

2.3.1 Foundations of Breast Cancer

Breast cancer is the most abundant cancer among women; it accounts for 25%[10] of all cancer cases (reported for women) and although survival rates in first world countries are about 80-90%, over 600,000 breast cancer related deaths occurred in 2018.[11] There are several risk factors that can contribute to the development of breast cancer, such as obesity, ionizing radiation, and alcohol consumption, however, only about 5-10% of cases are due to the genetic inheritance of the BRCA1 and BRCA2 genes.[12] While the BRCA1 and BRCA2 genes are well studied and their relationship to breast tumor formation is understood, most cases of breast tumors are unpredictable as the relationship between risk factors and tumor formation are not well established and quite arbitrary. Since breast cancer is unpredictable yet abundant amongst women of older age, it is important to accurately detect the presence of malignancies when annual screenings are performed.

To understand the development of breast cancer, it is important to understand the anatomy of the breast. The main components of the breast are the areola, Cooper's ligaments, mammary gland, the nipple, and the retromammary space. A major component is the mammary gland, which contains sub-components; the lobules are connected by the lactiferous ducts and the ducts end in terminal end buds.[13] The mammary alveolus are small sacs located in the mammary gland that produce and store milk and they are clustered into groups called mammary lobules.[14] A cross-section of the breast and mammary gland structure is shown in **Figure 1** with the corresponding components listed. The blood vessels are excluded from the figure.
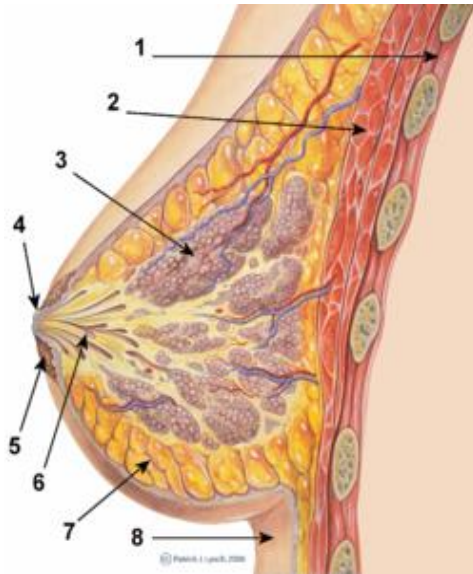
Figure 1[15]: Cross-section of a human mammary gland.

The various components of the breasts are as follows:

1. Chest Wall: the boundary of the thoracic cavity.

2. Pectoralis muscles: compose a bulk of the chest muscles and lie behind the breast

3. Lobules: they compose of lobes and they are connected by milk ducts

4. Nipple: where the milk leaves the breast through the lactiferous ducts

5. Areola: Surrounds the nipple

6. Milk duct: converge and forming of the branching of the lobes into the nipple.

7. Fatty tissue: loose connective tissue made-up of adipocytes. It also contains fibroblasts, preadipocytes, vascular endothelial cells, and many immune cells like macrophages.[16]

8. Skin: thin layer of skin that surrounds the breast.

Other components of the breasts that are not listed in **Figure 1** include the arteries, internal thoracic vein, axillary vein, intercostal nerves, supraclavicular nerves, intercostal nerves, and pectoral axillary lymph nodes. The exact composition of each feature is not exact, however, from BI-RADS, information on percent composition can be extracted. While there are four categories of breast density listed, **Table 1** demonstrates two general breast composition categories: dense and non-dense. From this data, the composition can be further split into the four categories by increasing/decreasing the stroma and fat, since stroma and fat compose most of the breast. For example, a breast with BI-RADS category 3 will probably have about 55% stroma composition, 4% epithelium, and about 41% fat composition.

Table 1: Percent composition of dense breasts versus non-dense breasts. The stroma includes the lobules and the connecting tissue.[17]

Breast Tissue Type	Dense Tissue	Dense Tissue	Non-dense tissue	Non-dense tissue
	Mean Area mm^2	Proportion %	Mean Area mm^2	Proportion %
Epithelium	1.21 (1.43)	5.6 (5.0)	0.14 (0.36)	1.07 (1.33)
Stroma	12.07 (6.17)	64.7 (17.7)	2.92 (3.57)	18.6 (14.5)
Fat	5.51 (4.27)	29.7 (18.5)	11.50 (6.0)	80.6 (15.8)
Epithelium + Stroma	13.28 (7.1)	70.3 (18.5)	3.06 (3.86)	19.4 (15.8)

There are two major carcinomas that occur in breast cancer: ductal carcinomas, which occur when malignant cells develop along the lining of milk ducts, and lobular carcinomas, which occur when the malignant cells develop around the lobules.[18] In addition, there are 18 other sub-types of breast cancer.[19] There are several sub-types of cancer but they can be categorized into five molecular classifications: ER+ (luminal A), ER+ (luminal B), HER-2/neu+, Basal-like/triple negative, and unclassified/normal breast-like.[20] In a paper written by Shahla Masood, the different types are described in detail. Luminal A cancer are HER2 negative and have low levels of Ki-67 and since they are low grade and grow slowly, they have the best prognosis out of the other cancer types. Luminal B subtypes are either HER2 positive or negative and they have high levels of Ki-67, thus making these types of tumors grow faster than type A. Because of this, their prognosis is slightly worse.[21] The Her-2/neu cancer types contain the HER-2 oncogene and are more aggressive (grow rapidly) thus result in poor prognosis. They are often associated with ductal carcinoma in situ, which means that the cells lining the milk ducts have become cancerous.[22] Basal-like breast cancers have distinct expression patterns and often don't express ER, HER-2, or PR, therefore some of these cancer types are also known as 'triple-negative,' however, cancers are specifically 'basal' when they are CK5/6+ and EGFR+. There is no approach to specifically target these types of cancer, but trials are underway for molecular targeted therapy. Basal-type carcinomas have the most distinct behavior out of the other molecular types and can be unpredictable; they vary in their response to chemotherapy and most

deaths associated with this cancer type occur within five years. They often lead to metastasis in the lung and the brain.

The five molecular classifications can be further narrowed into molecular characterizations. Invasive ductal carcinomas express about 50-80 percent of breast cancers and they don't exhibit any special morphologic features. The 'special' types of cancers compose 25 percent of cancer types. One of these is invasive lobular carcinoma. The other types are apocrine carcinoma, medullary carcinoma, adenoid cystic carcinoma, metaplastic carcinoma, infiltrating ductal carcinoma, mucinous carcinoma, invasive cribriform carcinoma, micropapillary carcinoma, neuroendocrine carcinoma, tubular carcinoma, glycogen-rich carcinoma, lipid-rich carcinoma, and secretory carcinoma. Of the lobular carcinoma types, there are a total of four: alveolar, pleomorphic (exhibit nuclear abnormality and are more likely to have HER-2 or p53 oncogene mutations), classical (characterized by single epithelial cell strands), and solid. Lobular carcinomas exhibit different metastasis patterns compared to ductal carcinomas and they exhibit more multifocality and bilatery.

Of the other cancer types, adenoid cystic carcinoma is difficult to detect because it rarely presents as an image-detected abnormality and instead shows myoepithelial cell differentiation. The apocrine carcinomas cannot be differentiated in breast tumors, but at a microscope scale, they exhibit glandular eosinophilic cytoplasm nucleoli. Infiltrating ductal carcinoma exhibits a round and well-circumscribed mass that is often sponge-like and firm; it may also contain calcifications. If accompanied with osteoclastic giant cells, this cancer type often involves the axillary lymph node. Medullary carcinoma, when imaged, appear as round or oval masses over 2 cm in length and they are similar to triple negative tumors. Metaplastic carcinomas can be further divided into properties they display: squamous, adenocarcinoma, and spindle cells. Micro-calcifications are common in imaging of this cancer type and they are often seen as firm, solid, well defined lesions. They also contain epithelial and spindle cell components, they have triple negative features, and they are aggressive. Micropapillary carcinoma occurs in the upper quadrant of the breast and appear to have an irregular mass and high density with certain regions of microcalcifications.[23] They range from a few millimeters to a few centimeters and about 80 percent of the

patients experience metastasis in the lymph nodes. Mucinous carcinomas are also known as colloid carcinomas and they are characterized by extracellular mucin and the prognosis is often favorable because of the biological markers present with this tumor type.[24] Invasive cribriform carcinomas appear with similar cribriform structures seen with ductal carcinomas in situ and they can be present with microcalcifications. They demonstrate favorable prognosis since they are not found to metastasize regionally or distantly. When neuroendocrine carcinomas are imaged, they appear as circumscribed tumors and the tumor cells are large with eosinophilic and granular cytoplasts. Tubular carcinoma can be image-detected as abnormalities and appear as a palpable mass; with a mammography, these tumors appear as a small lesion with microcalcifications and a central density.[25,26]

Tumor development requires biological resources and for this reason, tumors lead to hasty vessel formation, also known as angiogenesis. A powerful angiogenic factor is vascular endothelial growth factor (VEGF) and it is essential for the formation of vascular endothelial cells.[27] Because tumors develop vasculature in such a short period of time, VEGF is upregulated during tumor development and growth. In an early study conducted in 1999, Valtola et. al. sought to investigate the overexpression of VEGF in breast tumors and to differentiate their expression with the expression in normal breast tissue. VEGF (the ligand) is induced by hypoxia and is the most abundant angiogenic polypeptide in primary breast tumors. VEGFR, or VEGF-receptor, 1 and 2 bind to VEGF, however, 3 does not bind to VEGF but plays an important role in vessel development in embryos. In adults, increase in VEGFR-3 mRNA has been found in metastatic lymph nodes.[28] Known ligands of VEGFR-3 include VEGF-C and VEGF-D where VEGF-C is a growth factor important for development of lymphatic vessels. VEGF-C mRNA is expressed in nearly fifty percent of breast cancers and other malignant tumors. Since VEGFR-3 is prominent in breast carcinomas, Valtola et. al. used it as a marker to study the lymphatic vasculature of breast carcinomas. The group stained the vessels and the intratumoral vessel density was quantified by number of vessels seen with a 400x magnification in regions with high vessel density.

The results of the study showed that in normal tissue, VEGF-3 expression in the capillaries of the intraductal stroma was very weak. Valtola et. al. quantified the VEGFR-3 positive vessel density in normal

breast tissue to range between 6 and 17 but with a median of 9. To differentiate between lymphatic vessels and blood vessels, a double-staining procedure was done on two intraductal carcinomas. Staining the PAL-E, and endothelial cell antibody, would help identify the blood vessels whereas lymphatic cells express VEGFR-3 and are PAL-E negative. In the carcinomas, they found the blood vessels stained positive for both the PAL-E and the VEGFR-3. To further test if the cancer cells were undergoing angiogenic growth, the tumors were also tested for Ki-67 (a protein), a known nuclear proliferation marker. Using double-staining, the results showed that several of the tumor cell (inside the ducts) nucleae were strongly positive for Ki-67. When testing for VEGF-C presence in cells with antibody staining, most of the carcinoma cells tested very positive for VEGF-C whereas VEGF-C was negative for healthy breast cells. For invasive breast cancer (cancer that has spread beyond the tissue of origin), VEGFR-3 positive (which were strongly stained) vessels were located in all the invasive ductal lobular carcinomas studied and they did not appear to form any specific distribution pattern. The vessel density inside the tumors was quantified to range between 9 and 56 vessels with a median value of 21 and a very low p-value of less than 0.0001 (Mann-Whitney statistical test) therefore proving significant results. These vessels also proved to be immune-reactive to the PAL-E antigen. While VEGFR-3 expression in normal capillaries is weakly expressed, it is found to be very prominent along the lining of tumor-filled ducts. These nucleae also contained Ki-67 and the endothelial marker PAL-E (those with no PAL-E were assumed to be lymphatic vessels). In summary, Valtola et. al. demonstrated that VEGFR-3 expression increases during tumor growth and that the newly formed vessels are in the immediate vicinity of carcinoma cells. The results show two main points; the first, in imaging, tumor growth can be found by targeting regions of newly formed, unorganized vessels, and two, radiopharmaceuticals (such as contrast agents), can contain VEGFR-targeting antigens to specifically target breast cancer cells.

Tumor formation varies based on the tumor type, but notable shared features include increased vessel density in the tumor site, thin vessel walls, and high-density masses. In a later section, the visualization of vessel density with contrast agents to evaluate tumor formation is discussed while this section will discuss the role of breast density in tumor imaging. So far, the four different types of breast

densities on the BI-RADS scale have been explained. It is important to mention that density plays an important role in sensitivity; breasts with higher density usually have decreased sensitivity (discussed in the next section) in tumor identification. In a study that investigates the role of ultrasound in dense breasts, Thigpen et. al. mention that sensitivity of mammography is reduced among women with dense breasts.[72] In BI-RADS category 3 and 4 breasts, dense tissue composes a majority of all tissue in the breast and when imaged, the dense regions appear as lighter regions. Mammography utilizes x-rays to image the breast and is therefore dependent on density differences because density variations produce variations in attenuation factors. Tumors tend to have a higher attenuation than fatty tissue and when tumors are found in breasts composed primarily of fat, they can be easily seen in a mammography scan. However, with dense breasts, the dense tissue and the tumors become harder to differentiate and radiologists can miss the identification of a tumor because it may appear no different than the dense tissue. Thigpen et. al. found that the sensitivity of mammography is about 85 percent. However, women with dense breasts will experience a mammography sensitivity of about 47.8-64.4 percent. Mammography compresses the scan into a 2D dimensional image and therefore information on the structural integrity of the tissue is lost therefore increasing the difficulty of breast tumor differentiation. Thus, other imaging modalities are being considered for the detection of breast cancer

2.3.2 Imaging techniques for breast cancer

Breast tumors can be imaged with a diverse panel of imaging modalities, such as digital mammography, computer tomography, magnetic resonance imaging, and tomosynthesis among others. These imaging techniques vary on the x-ray energy used (if used at all), the signal processing tools, angle used, and robustness. Their efficacy is quantified by their sensitivity and specificity and in cases where an imaging technique does not provide enough information, it is often supplemented with another technique that can provide extra information. Sensitivity is defined by the probability of a 'positive' result, given that the sample (patient) is a true positive (has a malignant breast tumor). The percentage for sensitivity is given by **equation 1** below:

$$sensitivity = \frac{number\ of\ true\ positives}{number\ of\ true\ positives + number\ of\ false\ negatives} \quad (eq.\,1)$$

The specificity quantifies the opposite; it provides information on the proportion of samples (patients) that will test negative while being truly negative (not diseased). The specificity is then given by **equation 2**:[29]

$$specificity = \frac{number\ of\ true\ negatives}{number\ of\ true\ negatives + number\ of\ false\ positives} \quad (eq.\,2)$$

When comparing the efficacy of different imaging techniques, the p-value of results is often calculated to show the significance of the results. Typically, a p-value of 0.05 is used to declare results as 'significant,' thus implying enough evidence to reject the null hypothesis. The smaller the p-value, the stronger the evidence against the null hypothesis; this often means that the alternate hypothesis (i.e. contrast enhanced mammography *is* better at identifying breast tumors than regular mammography) is likely true. Several studies compare the sensitivity and specificity of multiple imaging techniques utilizing the p-value demonstrating the significance of the results. Before the results of those studies are discussed, some background information for each imaging technique used in breast imaging is provided in the next few paragraphs.

Mammography is used specifically for the purpose of diagnosing and screening breast tumors. The process involves using low energy x-rays of no greater than 40 kVp and the goal is to locate micro-calcifications or other signs of breast cancer. The procedure involves compressing the breast (typically one at a time) with parallel plates that evenly distribute the thickness of the breast tissue. This step is necessary to reduce the amount of scattering and to reduce motion blurring. The x-ray beam is located over the top plate and the film plate is located at the bottom. Images of the breast tissue are collected from the craniocaudal view (top to bottom) and from the mediolateral oblique view (angled side-view). Over recent

years, mammography has been performed digitally therefore replacing x-ray film with digital receptors and computers; this allows radiologists to manipulate the images to make the resulting images clearer.[30] This imaging modality is usually followed up with a more accurate imaging modality, such as MRI, for further screening if the mammogram shows questionable findings.[31] Mammography has a disadvantage in that it does not differentiate cancerous tissue from dense breast tissue very well, resulting in a false-negative rate of at least ten percent.[32]

In ultrasound medical imaging, high-frequency broadband sound waves are reflected in tissue with the receipt sound waves which are then used to create an image of the differentiated tissues. The ultrasound receiving signal can be described by a set of reflection and transmission coefficients that are unique to the tissue structure.[33] Compared to computed tomography and MRI, ultrasound provides less anatomical detail, however, it does not emit ionizing radiation (unlike computed tomography), is relatively inexpensive (unlike MRI), and provides detail on moving structures in real-time. Although ultrasound can be performed with or without a mammogram, it is often paired with a mammogram to supplement detail provided with the mammography.[34] Ultrasound can be enhanced with the use of microbubbles, which bind to targeting ligands that can bind to specific receptors that are characteristic to the disease of lesion of interest.[35] Although contrast-enhanced ultrasound techniques have not been approved by the FDA, studies have shown contrast agents for ultrasound are safer than the radiocontrast agents used in computed tomography scans, both in children and adults.[36]

Magnetic resonance imaging, or MRI, is an imaging technique that utilizes magnetic fields instead of radiation to image organs or other anatomical features. The magnetic field utilizes the hydrogen in the body to create a signal and the higher the hydrogen concentration in a region, the higher the signal. Since MRI scans do not use ionizing radiation, they have the least risk associated with them compared to the other imaging techniques listed here.[37] While imaging techniques that utilize x-rays produce images of structural components, such as the skeletal system, MRI has the ability to show metabolic function, such as brain function and injury, as well. The variability of MRI imaging is selected through the choice of sequence. The MRI sequence is the setting for which radiofrequency pulses and gradients are selected.[38] For breast

tumor imaging, MRI has shown a substantial increase in tumor detection, however, the sensitivity, especially with contrast-enhancement (discussed later), is much greater.[39] Although MRI is seen as a better imaging modality than computed tomography, the scans take a longer period of time and they are louder, therefore patients receiving an MRI might be prone to discomfort. MRI scans are also costlier and are not seen as a first-choice diagnostic tool.

Computed Tomography, or CT, is an imaging technique that utilizes computer-generated x-ray measurements from multiple angles to create tomographical images, or slices, of the scanned area. Digital processing allows for a 3-dimensional view of the interior of the body.[40] CT has become very popular over the last two decades due to its ability to provide detailed images with high resolution. In fact, CT can distinguish tissues with density differences as low as 1%.[41] Unfortunately, CT scans deposit rather large amounts of radiation therefore they are overlooked as a method for breast tumor diagnosis. The dose far exceeds that of mammography therefore CT is not a savory alternative although the diagnosis would improve. A better alternative to CT is an imaging modality that utilizes similar technology as CT but does not impart as much dose. Over the last few years, a new imaging modality known as tomosynthesis utilizes similar technology as CT, but only over a limited angular range, thus significantly decreasing the dose.

Tomosynthesis is an imaging method that combines aspects of high-resolution mammography and computed tomography. The high-resolution necessary for mammography was achieved with the development of a flat panel digital detector.[42] Similar to computed tomography, tomosynthesis acquires 'slices' over a region of interest, however, it is done over a limited range instead of an entire 180-degree rotation. This has tokened tomosynthesis as a low-dose alternative to computed tomography.[43] In terms of reconstruction, tomosynthesis utilizes reconstruction algorithms similar to CT, however, since tomosynthesis does not acquire full anatomical 'slices,' approximation algorithms are used instead. Two prominent algorithms used for tomosynthesis reconstruction include filtered back projection and iterative, expectation-maximization.[44] Over recent years, the use of tomosynthesis for breast imaging has been under development. While early studies showed very little improvement of breast imaging with tomosynthesis, later studies recognized that dual-view breast tomosynthesis paired with mammography provide advantages

over plain mammography.[45,46] If tomosynthesis is used as an extension to mammography, the detection rates increase with little increase in radiation dose.[47] In addition, as radiologists become more experienced with reading tomosynthesis images, the detection rate is expected to increase.

One of the latest methods for breast tumor imaging is Digital Breast Tomosynthesis, or DBT. In a study conducted in 2018 titled *Role of tomosynthesis in breast imaging going forward*, Michell and Batohi[48] find that using DBT to identify breast tumors shows an improvement in the assessment of tumor size and an improvement in sensitivity when compared to 2-D digital mammography, or 2DDM. In this study, Michell and Batohi describe DBT as a technique involving acquiring several images over a limited angular range with the goal of producing a 3D reconstruction of the breast. This is an advantage over 2DDM because 2DDM's limited 2-dimentional perspective can be difficult to interpret as the overlapping images cause obstruction and confusion of the multiple present tissues. DBT functions similarly to 2DDM but is modified so that the low-dose projection images only occur through a range of about 50-60 degrees.[49] The several images are then 'stacked' at intervals of about 1mm to create a 3D image. This 'stack' of images does not result in the superimposition of multiple tissue, an advantage over 2DDM.[50] The DBT technique also varies from computer tomography in that it does not contain features from adjacent layers.

In their study, Michell and Batohi found that DBT has a greater ability over 2DDM to identify the features soft-tissue lesions therefore providing better local staging as well as diagnostics.[51] This was particularly improved for women with dense breasts. The increased ability to define benign tumors over cancerous ones in DBT also means that the need for biopsy can be eliminated.[52,53] The study also discussed that DBT provides a more accurate estimate of tumor size compared to 2DDM, but DBT does not always predict the accurate size of invasive lobular carcinomas. For multifocal breast cancers, MRI currently stands as the reference for breast cancer staging.[54] Michell and Batohi also cite other studies where the improvement seen in DBT compared to 2DDM are quantified. In the TOMMY trial, a study involving 7,060 participants, DBT paired with 2DDM showed an improvement in sensitivity for women with dense breasts compared to 2DDM alone. The results demonstrated 93% sensitivity for the DBT-2DDM combination and an 86% sensitivity for 2DDM alone. These results yielded a p-value of 0.03 and the participating women

had breast densities of 50% or more. Specificity also improved from 57% to 70% from 2DDM alone compared with 2DDM supplemented with DBT.[55] Michell and Batohi also pointed out that prospective trials demonstrated that pairing 2DDM with DBT increased the detection of invasive cancer but no significant increase in the detection of in situ carcinoma. While Michell and Batoni demonstrated the multiple ways that tomosynthesis improves breast tumor detection, they point out that the improvement is difficult to quantify because optimization of tomosynthesis is dependent on several factors, including breast density, tumor type, exposure time, amongst others. For this reason, there are no established standards on DBT operation. The parameters determine dose to the patient as well as image quality, therefore it is important to evaluate how each parameter affects the resulting image.

In a different study conducted in 2013, Thibault et. al. compared the performance of five different imaging techniques.[56] The techniques utilized a combination of breast tomosynthesis, or BT, dual-view mammography (DM), and breast ultrasound (BUS). In summary, the study involved 130 patients, 55 of which contained malignant tumors and 76 contained benign tumors and normal cases and the imaging techniques were: DM, DM+ BUS, DM + US + BT, and BT + DM. The performance of the different imaging techniques was evaluated with receiver operating characteristic analysis (ROC). When presented to radiologists for evaluation, the images were presented in a different order to reduce memory bias of the same person. The radiologists evaluated the scans with the Kendall's coefficient of concordance for ordinal response and assigned a value of 0.6+ to indicate if results are significant. The results demonstrated the highest coefficient of concordance for the DM + BT and the DM + BT + BUS techniques. In addition, all the coefficients had p-values of less than 0.001, thus considering them statistically significant. The techniques that demonstrated the highest sensitivity were BM + BT + BUS and DM + BUS, however, they also demonstrated reduced specificity. The highest values of the AUC-ROC (which helps indicate a models' capability to distinguish between classes[57]) curve occurred for BT + DM and BT + DM + BUS readings.

The results showed that BT was not inferior to DM but that BT + DM was not proven to be superior to DM or DM + BUS. In a bootstrap approach conducted by the team, DM + BT + BUS was shown to be superior to DM + BUS, however, the other two robust models used to evaluate the technique performances

did not back up the evidence. The results of the study do not agree with a different study conducted by Svahn et. al.[58] that found evidence supporting the theory that tomosynthesis provided significant advantages to the other imaging techniques. The study conducted by Svahn et. al. found that breast tomosynthesis outperformed DM in sensitivity as well as diagnostic accuracy. They also found that BT did not result in significant decrease in specificity, which also contradicts the results of Thibault et. al.. A difference between the Thibault et. al. study and the Svahn et. al. study is that the latter utilized image readers that belonged to the same institution, therefore reducing variability in the results. Thibault et. al. recognized that a significant fault in the study is that the readers were not as experienced in reading tomosynthesis images as they were reading DM and BUS images; experienced readers in tomosynthesis increase the technique's sensitivity with a similar, or slightly improved specificity.[59] Another fault in the study was the use of bootstrapping data to compensate for lack of patient data, which resulted in twice the increase in margin of error. Although the results might have been biased, Thibault et. al. recognized the tomosynthesis has potential to increase the visibility of malignancies and might be able to recognize microcalcifications missed by other imaging techniques.

2.3.3 Common use of Contrast Agents in Imaging

The use of contrast agents for diagnostic imaging serves a broad purpose across multiple imaging techniques. Contrast agents have been used in computer tomography and MRI and recently, they have been proposed for digital mammography. While contrast agents have been used to enhance the visibility of tumors during diagnostic imaging, they can also be used to enhance other features, such as vasculature and calcifications. The use of contrast agents in medical imaging is an ongoing, explorative technique and there are several factors to consider when creating contrast agents, such as, is the effective 'Z' comparably higher than the effective 'Z' of the surrounding tissue? Is the contrast agent compatible with the imaging modality? Can the compound be metabolized without inducing toxicity? Does it have a strong affinity for tumors or some other target component? While keeping these questions in mind, researchers have developed contrast agents for specific use (per imaging modality) and the following work describes the utility of these contrast

agents for tumor visibility. Although contrast agents are experimented with in the initial stages of this project, their discussion is important in order to understand the mechanics in tumor visualization and how this can be incorporated into a phantom model.

An early application of contrast agents was the use of gadolinium in magnetic resonance imaging. In a paper titled, *Gadolinium-DTPA as a Contrast Agent in MRI: Initial Clinical Experience in 20 patients*, D. Carr[60] describes the experimental use of gadolinium-diethylenetriamine pentacetic acid as a contrast agent in conjunction to MRI. In this experiment, the target organ was the brain and a few of the subjects had metastatic tumors elsewhere in the body. Gadolinium^{+++} contains seven unpaired electrons and is able to facilitate MRI relaxation. Generally speaking, MRI contrast agents need to have paramagnetic elements, such as manganese, iron, chromium, and gadolinium. Although these elements are toxic on their own, they pose no threat to health is they are chelated with acids or other molecular structures.[61] In this experiment, gadolinium was chelated with DTPA, which is a compound used to minimize the amount of time a metallic element spends in the body. Therefore, any gadolinium that is injected into the site of interest can be metabolized. In order to increase the tumor affinity of the Gd-DTPA compound, the gadolinium is introduced to tumor-specific ligands. A common cell receptor to target is the HER-2/neu receptor, which is part of the epidermal growth factor type and this receptor if over-expressed in several cancer types.[62] Therefore, if the Gd is paired with an antibody that targets this receptor, then the Gd-DTPA will be absorbed at a higher rate in the tumor than in the surrounding tissue.

In the experiment, Carr administered the contrast agent via injection with a dose of 0.1 mmol/kg of body weight. Following injection, a series of MRI scans operated at 0.15T were performed within 65 minutes of administration. The scans used saturation-recovery (SE), inversion-recovery (IR), and spin-echo pulse sequences. Image reconstruction was performed with either projection reconstruction or 2D Fourier transform. Base MRI images were collected prior to contrast-agent enhancement and they were used to compare the visibility of the tumor before and after contrast enhancement. For those with cerebral tumors, all tumors displayed enhancement with the contrast agent in the form of lightness (brightness) increase in both SE and IR sequences. Although the contrast agent was more notable with the IR sequences in MRI

than in the SE sequences, it was more difficult to differentiate between the tumor and parenchyma. After 48 hours, there was no increase in enhancement of metastatic adenocarcinoma to the liver. While hepatic cysts were not enhanced, they became more notable with the enhancement of the normal liver. There was enhancement in lesions in the spleen in patients that had metastases from colon and lipoma carcinoma. The contrast agent caused no side effects and the results of the test demonstrated no elevated levels of creatine and electrolytes and no toxicity was shown. In the study, contrast agents proved to be a useful supplement to MRI because of its potential to speed up the process by decreasing the T1 recovery time, thus allowing for a higher pulse rate.

Although contrast agents in MRI applications need to show paramagnetic properties, imaging that utilizes ionizing radiation, such as computer tomography, benefits from the use of contrast agents that increase the effective 'Z' of the target. This means that the contrast agent should contain 'heavy' elements that have good attenuation properties and can provide a distinguishable difference between photon absorption in healthy tissue and absorption in the tumor.

In a study conducted by Caschera et. al., contrast agent performance was evaluated for computed tomography (CT), ultra sound (US), and MRI.[63] For these various imaging modalities, the enhancement in a region due to contrast agent is directly proportional to the concentration of the contrast agent, therefore, high uptake of the contrast agent represent a high-interest region. The three physiochemical properties of contrast agents identified in this study were concentration, viscosity, and osmolality. Contrast agents for CT focus on increasing the absorption of x-ray radiation in the target organ, lesion, or blood vessel. Iodine is the most popular element to use for CT contrast agents because of its K shell binding energy of 33.2 keV, which is close to the average energy used for medical diagnosis imaging, thus providing an increase in attenuation in the regions it is absorbed in. Caschera et. al. estimated that the average increase in attenuation in the target tissue is 25 Hounsfield (HU) units for each mg of iodine per ml of blood or mg/cm3 of tissue.[64] Ultrasound imaging provides "live action" information on vascularization of tissue based on the Doppler technique and contrast agents for US allow for tissue perfusion imaging. The first contrast agents were encapsulated air microbubbles but they would dissolve before reaching the vascular network, therefore, the

addition of phospholipids helped provide structural stability.[65] Contrast agents in ultrasound work by increasing the frequency of the vasculature they are contained in and since their development, there have been diagnostic applications in liver imaging for characterization and assessment of lesion detection accompanied with a treatment response. Contrast agents for MRI work by increasing the proton relaxation rates in the area of interest which then shortens the T1 and T2 (relaxivity). The contrast is represented by the T1 and T2 ratio and T1-specific contrast agents are composed of paramagnetic complexes while T2-specific contrast agents are composed mainly of super-paramagnetic ions. Therefore, MRI contrast agents can vary based on their application and can be used to highlight different regions of the target tissue. For these various types of contrast agents, the chelating compound is important so that the delivery of the contrast agent (whether it be iodine for CT or gadolinium for MRI) reaches the target location in high quantity.

For the purpose of this paper, the focus will be on contrast agents for CT, since tomosynthesis also utilizes x-rays and the contrast difference is dependent on the effective Z of the tissue being imaged. A method for tumor identification in breast cancer during tomosynthesis, or other x-ray form of breast imaging, is using contrast agents to evaluate tumor angiogenesis in the breast. In a study conducted in 2006, Dromain et. al. evaluated tumor angiogenesis in breast carcinoma using contrast-enhanced digital mammography.[66] As discussed earlier in this paper, angiogenesis is associated with tumor growth and microvessel density has become an important step to evaluate cancer progression in a patient. Contrast-enhanced digital mammography and MRI techniques are being used to explore angiogenesis in breast carcinoma. These techniques show an increase in improvement of tumor detection and characterization, but MRI has limited specificity, is expensive, and has restrictive access. For these reasons, contrast-enhanced digital mammography is being explored as a means of imaging breast tumors over MRI. The study focuses on testing the accuracy of contrast-enhanced digital mammography, CEDM, and correlate the findings with those of histologic analysis using microvessel quantification. The women's breast densities were categorized with BI-RADS; 11 patients were category 2, 8 patients were in category 3, and 1 was in category 4. To perform CEDM, a Cs-I-amorphous silicon flat-panel detector was used, and the radiograph spectrum

was shaped to be just above the k-edge of iodine (33.2 KeV). To introduce the contrast agent into the patient, a catheter was injected into the antecubital vein of the arm located contralateral to the breast being imaged. Each breast was compressed with 5 daN to prevent motion artifacts. The contrast agent used was 100 mL of Omnipaque 300, nonionic contrast. Afterwards, the images underwent histologic analysis; first, the vascular density was approximated using anti-CD34 immunochemistry. Tumors were evaluated using a five-step procedure: background correction, tissue detection and necrosis elimination, immunostained structure detection, hot spot identification, and measurement.

The results showed successful CEDM tumor identification in 18 patients and failed in 2 patients. The 2 patients had tumors located by the pectoral muscles, therefore they were out of the field-of-view. After calculating the statistical significance of the results, it was concluded that CEDM has a sensitivity of 80%. The results of the study demonstrated that angiogenesis is heterogenic across different tumors hence demonstrating different reactions to CEDM. Although vessel density seems to play a role in detection, the quantity of vessels is unimportant when compared to the vessel characteristics, such as permeability (tumor-created vessels have thinner walls compared to healthy tissue vessels). When compared to MRI, CEDM provides worse contrast resolution as well as inducing unwanted ionizing radiation. However, since the technique is easy to implement, contrast agents should be complimentary to breast mammography for it provides visibility to lesions that remain hidden under simple mammography.

There are several contrast agents available for CT; most of them contain iodine. In an American Chemical Society publication, Lusic et. al. wrote an extensive review on the x-ray computed tomography contrast agents currently available as well as those under development.[67] In the review, Lusic et. al. mentions the chemical requirements and the biological requirements for the proper function of contrast agents, as well as elements that provide good contrast in biological media. The contrast material should have a high density (ρ) or high atomic number (Z) to increase x-ray absorption, known as attenuation. The factor for the absorption coefficient is given by **equation 4**:

$$\mu = \frac{\rho Z^4}{A * E^3} \quad (eq.\,4)$$

where the A is the atomic mass and E is the energy of the incident x-ray. If the incident x-ray energy is equal to or greater by a small margin than the k-shell binding energy of the electron in the target atom, a significant increase in attenuation (absorption) coefficient occurs. The energy value at which this occurs is known as the k-edge, or absorption edge; this value increases with atomic number. If contrast media is used during an imaging session, the radiologist will use an x-ray energy that closely matches the k-edge of the main element used in the contrast media.

In order for a contrast agent to serve its purpose, the contrast agent needs to: increase the sensitivity of CT and provide significant differentiation of the interest of tissue, provide evaluation of tissue performance, or provide biochemical information on the target tissue. Requirements for contrast agent approval include: readily soluble or stable suspension formation in aqueous (physiological) conditions with low viscosity, sufficient tissue retention for completion of an imaging scan, high mole percent of the dense element per 'vehicle' agent, relatively short clearance time (several hours instead of days), increase differentiation of the target tissue by at least a two-fold, be able to locate the target tissue and have favorable distribution in this tissue, and be nontoxic. One of the most common elements in CT contrast agents is covalently bound iodine due to its high atomic number. Nonionic iodine is preferred over ionic iodine because of its low osmolality, which does not cause renal toxicity and does not interact with biological structures like ionic iodine does. The structure of the iodine-containing molecule (or other heavy-element of choice) needs to be structured a certain way to fulfill the requirements of a contrast agent. To fulfil the solubility requirement under physiological conditions, the molecular structure often contains hydrogen-bonding hydroxyl. The prepared solution should also have low viscosity for easy administration and low renal damage. High stability with low toxicity of iodine can be achieved with an aromatic molecular structure; increasing the aromatic structure to two structures through covalent bonding also increased the iodine count per molecule. However, this increases the viscosity.

Currently, iodine contrast agents that demonstrate low binding to biological receptors, good water solubility, low toxicity, and biotolerability include ioxaglate, iodixanol, iothalamate, iohexol. Iopromide, and iopamidol. Recent studies have been conducted to increase tissue targeting of contrast agents. Iotrolan and iodixanol are clinically approved and have low-osmolality, are nonionic, and are two-ring, however iosimenol shows a much lower viscosity than iodixanol but is still being evaluated for clinical trials. To use these iodine contrast agents as targeting agents, conjugation between iodobenzene and phosphonate/peptide can help increase targeting, especially in the gastrointestinal region. To reduce the clearance time and increase blood residence time, nano-sized contrast agents are being proposed as a solution. [68] Nanoparticles can be created in a variety of forms, including nanosuspension, microspheres, liposomes, polymeric particles, nanoemulsion, liposomes, and nanocapsules. In addition, the nanoparticles can contain other heavy elements, such as gold, silver, bismuth, among others, that can provide a higher attenuation than iodine. These different elements are currently being explored as viable contrast agents for medical imaging. The size of the nanoparticles can help determine the delivery of the pharmaceutical, for example, nanoparticles of size greater than 400 nm are taken up by macrophage cells. While the potential side effects of iodinated nanoparticle contrast agents pose a significant challenge, controlling the charge, size, and composition can help reduce the harmful physiological response associated with the agent while optimizing its benefit.

2.3.4 MCNP Simulations

For decades, research projects have utilized computation anthropomorphic phantoms to simulate the interactions between radiation and the human body. These simulations are responsible for considering every interaction that occurs between the radiation particle or photon and human cells. A general-use code that is commonly used for these simulations is Monte Carlo N-Particle, or MCNP, which is a radiation transport code designed to 'track' a range of particle types over a large range of energies based on several conditions.[69] The most current version of MCNP is MCNP6.2 which is similar to its predecessor, except it contains new features, such as improved physics, data, source, tallies, and unstructured mesh capabilities.

This project utilized three key aspects of the Monte Carlo code; the first aspect is the source simulation and the resulting radiation interactions (radiological), the second aspect is the anthropomorphic phantom which included an accurate biological representation of tumor growth in the breast (biological), and the third aspect is the imaging results which simulated the resulting scan that a radiologist would produce at a hospital (imaging). While the first and third aspects are straight forward, the second aspect has much to consider, in particular, what phantoms are best suited for creating a realistic breast phantom. While voxel phantoms have been used for decades, the new version of MCNP allows researchers to use mesh phantoms, structured or unstructured. The variety of phantoms provides several choices to choose from and the optimal choice is dependent on the project type. The next few paragraphs discuss the differences between the phantom types and information on the optimal settings for this project.

In 2003, a group of researchers performed a review of multiple anthropomorphic phantoms and compared them based on accuracy and robustness.[70] In the review, Lemosquet et. al. discussed the anthropomorphic phantom models to calculate dose from ionizing radiation and the models used were based on CT and MRI images used as references. One of the earliest used references for phantoms is from The Visible Human Project.[71] The Visible Human Project was a project done by the National Library of Medicine from 1994-1996 that created public data on human body anatomy. The project published data of both a male and female cadaver with transversal slices of one millimeter for the male and one third of a millimeter for the female. A few years later, Spitzer and Whitlock created an anatomical atlas based off of The Visible Human Project. The resulting data from this project was used to create various phantoms, including the VIP-Man, Reduced Visible Human, and Meetman.

The VIP-Man was created in 2000 by Xu et. al. and it utilized the images available from The Visible Human Project to preform dose calculations in various organs from several different radiation products.[72] Xu et. al. utilized different computer programs to create voxel phantoms, among them EGS4 and MCNPX. The group reported a finer resolution for the EGS4 phantom due to smaller memory requirements, thus reducing the voxel size to 0.33mm x 0.33mm x 1mm. However, MCNPX did not have the same memory capabilities and the voxel size was increased to 4mm x 4mm x 4mm thus reducing the whole-body

resolution. The Reduced Visible Human, created by Aldridge et. al. was created as a 'standardized' phantom for the purpose of radiotherapy.[73] The phantoms were used for research in intensity modulated radiotherapy but since the calculations used to create the phantom are based on convolution algorithms, the calculations are not considered Monte-Carlo type. The MEETMAN project, which was in the works from 1996 until about 2000, used The Visible Human Project images and other CT images to create extensive data on the properties of the human body. According to Sachse et. al.,[74] the phantom's purpose stretched beyond the effects of ionizing radiation and included the study of electromagnetic fields and the thermal properties of the human body. Other medical applications studies with the MEETMAN include segmentation of the heart and the resistance of biological material. The resolution of MEETMAN varies from one to eight millimeters therefore allowing the user to choose resolution based on memory capabilities. In 1997, Lawrence Livermore National Laboratory obtained anatomical information from MRI images and created a software package called Magnetic Resonance Imaging Photon Phantom (MRIPP) which write an MCNP-format input file that is dependent on the required geometry. The resulting database contains 33 voxel phantoms and the voxels in each model represents a cell where the material of that cell is reduced to only air, bone, or soft tissue.

Although there are several voxel phantom models available to the public, they each contain an important tradeoff between voxel size and anatomical accuracy. The smaller the voxel size, the higher the anatomical accuracy, *however*, the higher the anatomical accuracy, the higher the memory uptake and the slower the simulation time. In a paper titled *Mesh Human Phantoms with MCNP*, Anderson et. al. compares the differences between voxel and mesh phantoms by taking existing voxel phantoms and converting them into mesh models.[75] In their work, Anderson et. al. used the latest release of MCNP to create unstructured mesh models using input files generated from Abaqus/CAE (computer aided engineering) which they claim provide faster computational runtime as well as improved geometry. In addition, a big advantage of mesh capabilities over voxel capabilities is that MCNP is able to perform multiphysics finite element analysis of the mesh. Because MCNP can incorporate hybrid geometries, the group used hybrid geometries with unstructured mesh human phantoms to compare dose calculations to those of voxel phantoms. The pre-

existing voxel phantoms used for the study include the VIP-Man, the Snyder Head, and the Zubal Head. The models were reconstructed into hexahedra mesh models with meshing tools provided by Abaqus/CAE. MCNP6 then reads the mesh data files generated by Abaqus/CAE to create a global mesh model created into a mesh universe. The mesh needs to be in a universe with constructive solid geometry for particle transport simulations, since particle tracking occurs in the constructive solid geometry universe and in the mesh.

To convert the voxel phantoms into mesh phantoms, Anderson et. al. used a python script to convert the voxel geometries into a mesh input file for Abaqus/CAE. While the Snyder head only took several minutes to run the python script, the largest MCNP lattice took up to three days. For the VIP-Man and the Snyder head, an unstructured mesh solid model was generated with Abaqus/CAE (lungs for VIP-Man) and then compared with the voxelized models. Both of the unstructured mesh models demonstrated computational improvements when compared with the voxelized models. While the unstructured mesh lungs computed in half the time than its voxelized counterpart, the Snyder head was also more geometrically accurate and faster than its voxelized counterpart. The mesh was able to tally the particle flux and the energy deposition incident upon the mesh tally, therefore, a direct comparison between the mesh and voxel phantoms count could be performed. The tallies showed statistical agreement for the various models created (both mesh and voxel) for the Snyder head but the larger models had some discordance, mostly due to the large number of elements in each model. The hybrid models took longer to generate than the models in constructive solid geometry and other model comparisons were still under development. The conclusion of the project is that unstructured mesh phantoms have great potential. Since mesh phantoms are a fairly new strategy, anthropomorphic accuracies are still being compared.

Although mesh phantoms and mesh tallies appear to be an improvement from voxelized models, a group proposed that lattice tallies are an improvement over mesh tallies. Zhang et. al. utilizes MCNPX explore the use of lattice tallies over mash tallies to reduce simulation times associated with proton therapy dose calculations.[76] A full body reconstruction was built for mesh tallies and for lattice tallies to quantify the agreement for dose calculations for both of the strategies. The group simulated dose reconstruction for

a patient receiving craniospinal irradiation with proton beam and to create the MCNP input files, they used a code that can simulate the proton treatment and run the simulations. The patient phantom was reconstructed based on CT images as reference. The voxel size used was about 4mm x 4mm x 5mm and the matrices of material composition and mass density values were created by converting the Hounsfield Unit values of the CT matrix. The Hounsfield unit (HU) represents a linear transformation of the linear attenuation coefficient measurements used in CT scans.[77] The HU values can be calculated with **equation 3** below:

$$HU = 1000 \times \frac{\mu - \mu_{water}}{\mu_{water} - \mu_{air}} \quad (eq.\,3)$$

where the μ represents the linear attenuation coefficient of the material.

For comparison purposes, the computational time, given in CPU-minutes, for both the mesh and lattice tallies, was characterized as a function of the phantom voxels and number of proton histories. The dose distribution of the models was compared with gamma analysis. The results demonstrated that the lattice and mesh tallies produced nearly identical dose distributions. In addition, the lattice tally proved to be about 4-17 times faster than the mesh tally and the calculation speed of the lattice tally increased with the voxel number. After about 10 million simulation histories, the calculation speed remained constant at about 6 times faster than the mesh tallies. A fault found with the mesh tallies is that it duplicated certain calculations performed by the particle-tracking algorithm; the transportation algorithm was found to calculate the location of the particle and calculate which voxel the mesh particle was located in thus duplicating the location calculation. The group found that the mesh tally doesn't assume congruence with the lattice mesh therefore reducing the mesh tally's efficiency. The lattice tally is also able to provide statistical information on the simulations performed thus providing a major advantage over the mesh tally. Although the lattice tally was faster than the mesh tally, the mesh tally has visualization capabilities; MCNPX allows plotting the superimposed mesh tally over the problem geometry while the lattice tally cannot be plotted. Overall, the study demonstrated superior computation speeds and statistical analysis

produced by the lattice tallies while still being able to produce accurate dosimetric results and provided evidence that lattice tallies will improve simulation capabilities.

MCNP can also be used to simulate a variety of imaging systems. For this project, tomosynthesis is the imaging system of interest and it is most similar to computed tomography. In a study that simulated a computed tomography system, Long et. al. validated organ dose studies with the use of physical phantoms.[78] The group simulated the Siemens SOMATOM Sensation 16 multi-detector CT scanner with a fan beam of 52 degree using MCNPX. The source from this system was able to simulate various parameters, including filtration, beam energy, pitch, and a beam collimator. To test this CT system, Long et. al. created two custom-built human phantoms; these were used for dose measurements. One of the phantoms was that of a 9-month-old and the other was an adult male. The adult phantom was a replica of a reference male hybrid phantom created by the University of Florida. The nine-month old was a replica of the university's voxel phantom of a nine-month old.

To build the source system, Long et. al. used the manufacturer data of the material and thickness of the Siemens CT system. To create the x-ray spectrum, Long et. al. used the commercial spectrum generation program SPEC78 created by the Institute of Physics and Engineering in Medicine to generate the spectra for the head; it was also used to generate the body filters at all beam energies.[79] To incorporate the spectra into the MCNP source model, the spectra was placed in as an input deck for energy sampling. Since the system had a bowtie filter on the fan beam shape, the effects on this filter were incorporated for all beam energies and filter combinations with angular-dependent weighing factors.[80] The model was created so that the user could simulate helical and axial exams of varying pitch. The helical exams were accomplished by having the source find the location of the x-ray focal spot lined along a mathematically defined helix based on the pitch scan length, which can be selected by the user. The source model created by Long et. al. adds half a rotation at either end of the scan length to account for over-ranging. For scans conducted in the axial range, the procedure was to sample the focal spot along a series of circular rings of radius 57 cm that span the total specified length of the scan with an axial scan. The source was then able to sample an angle within 52 degrees of the fan beam as well as within the thickness of the collimator to select

an initial photon direction. The photon energy of the scan is then an energy based on the spectrum range. This process is repeated for every particle transported.

The CT MCNP system was then used on the adult phantom model; organ dose measurements were taken at 6 different CT scan protocols. For the scan simulations, the phantom's environment was a vacuum-locked immobilization bag that aligned with the CT scanner's axis of rotation. The CT scan table was modeled as two carbon-fiber concentric cylinders. The dose was collected in dose tallies and then converted into units of Grey. The results demonstrated that the helical scans had larger percent variance than the axial scans; this is probably due to the fact that the helical scans had over-ranging and starting angle artifacts. The results demonstrated that the differences in dose to the organs did not exceed about ten percent of the actual dose while acceptable dose differences are values within 20 percent.[81] Errors in dose calculations were assumed to be due to MCNP tally error. Overall, the MCNP CT model proved to be an accurate delivery of dose to patients for dosimetry calculations.

Since MCNP phantoms are often used for dose calculations, there aren't many resources on the use of MCNP to generate radiograph images. In a study conducted in 1998, Peplow et. al. explored MCNP's capabilities for modeling mammographic Images.[82] Peplow et. al took advantage of MCNP's nested geometries that are commonly found in mammographic phantoms. To conduct the study, Peplow et. al. used an American College of Radiologists test phantom and a contrast detail phantom. To create the images, Peplow et. al. used the point detector scheme with an internal version of MCNP. Each particle in the simulation is scattered along a photon path through the geometry and given a probability of landing on a pixel along a grid. The result of this method is a finite score of every pixel in the image in each history, which helped lower the variance. To make the point detector scheme suitable for calculating realistic radiographical images, Peplow et. al picked the same number of photons that are picked in the direction of each detector pixel; this is called source rastering. Another technique was to separate the scattered photons from the unscattered photons. The unscattered photons could just go directly to an aligning pixel while the scattered photons experienced large attenuation changes as they traversed through the geometry. The scattered and unscattered images could then be combined. Finally, the image was created by applying the

modulation transfer function to the image. The image score was assigned based on the number of differentiable objects from the imaged 'tablet.' The results demonstrated nearly the same score between the MCNP-created radiograph of the tablet and the Fischer Senoscan machine-generated image. A slight artifact that was present in the MCNP-generated image that was not present in the Fischer image was a whitening effect seen at the top of the image. This is due to photon flux variation that is corrected with Fischer technology.

Although there are not that many studies that have used MCNP to produce radiographical results, techniques that use MCNP to simulate the interaction of photons with various material are widely available. In addition, the MCNP6.2 manual provides bountiful resources on the availability and limitations of mesh phantoms as well as geometric capabilities. With MCNP, various scenarios can be simulated; this includes modifying various input decks, such as the energy of the incident beam, the target material, which is useful for testing out various contrast agents with different attenuation coefficients, and scan angle range among other modifiable factors.[83] A python script can help generate the input script for Abaqus, or other related software that can create the mesh environment to create an anthropomorphic model of healthy breasts and tumor-filled breasts. A different script can help create the settings for a tomosynthesis simulation with varying energy spectra and create the input deck for MCNP. Finally, the results of the tomosynthesis simulation imparted on the mesh models can be imaged with a radiography simulation. This will demonstrate the performance of tomosynthesis on various breast tumor locations, breasts densities, and other conditions.

<u>3 Materials and Methods</u>

The majority of this project is computer based – simulations are used in place of real scans to create empirical data. Therefore, the materials and methods used for this project compose primarily of software and scripting tools to build a simulated model. Three main tools were used to construct the simulation: Python, Abaqus/CAE, and MCNP6.2. Other supplementary tools include Atom.io which is a graphical user interface to write Python scripts with, and the MobaXterm terminal with remote access to Unix servers

hosting MCNP6.2. Results generated by MCNP6.2 were visualized with Python as well. Atom.io is essentially a text editor so it is also used to write the MCNP input scripts and can be used to open and read MCNP output files. In this section, detail will be provided describing the equipment, strategies, and workflow used to construct the simulation. It will also include minor detail on materials and methods that will be included in the prospects of this project, however, more detail will be covered in the **Future Prospects** section of this paper.

3.1 Materials

Abaqus uses the finite element method to simulate different physics on given geometric models. There are seven steps required to create a finite element method (FEM) simulation: modeling, material definition, definition of loads, boundary conditions, meshing, solution, and post processing.[84] The first step, modeling, is self-explanatory and involves creating the geometry of the problem. Abaqus contains different construction capabilities for both 2D and 3D modeling, including extruding (applicable to 3D geometries), polygon creation, replication, among several others. The next step is material definition which includes defining the material properties, such as the density and elasticity, for the different materials present in the model. Defining the loads involves defining the different forces that are acting on the geometry, including any stress such as compression. The fifth step, meshing, is the step that creates the mesh defining the geometry. This step essentially 'breaks' up the geometry into finite elements and this step is what is going to create the mesh cells in the MCNP6.2 code, which will be discussed later. The solution step makes the code that represents the equation in terms of matrices. These are assembled into global matrices for the whole geometry then solved by finite element solvers. Finally, the post-processing step involves creating results that can be visualized through contour plots or graphs.

All these steps can be written into a Python script and then input into the Abaqus graphical user interface to produce results. The python script, which can be written in a text editor and, in this project specifically, Atom.io, can include everything that Abaqus needs to create the model. The general workflow of an Abaqus Python script is to create the model, create the individual parts, define the material properties,

define each section and assign the parts to their corresponding location, define the instances in the model, apply the loads and the boundary conditions, apply the mesh, create the job submissions, then apply postprocessing. While the model can be built directly with the Abaqus graphical user interface, there are several benefits to using Python scripting as a tool for model creation. Each part and junction are defined individually in Python and each part can be replicated and then modified to create several similar components. In addition, since Python is a programming language, functions, including built-in functions, can be written to facilitate creation of part components based on given conditions. This utility is especially useful when integrating the biophysics into the model. The first component of this project involves creating a basic model that replicates tomosynthesis on an average breast and outputs the radiographical image. Eventually, the project will involve developing and simulating several tumor types as well as incorporating contrast agents, and this is discussed in detail later. Python is an object oriented programming language and so it is especially useful in this project because there is an object of interest, a modeled breast, that will vary based on provided conditions and to implement the different conditions, the object must be modified to reflect the wanted conditions. Therefore, a set of functions are defined that alter the object based on provided inputs and this prevents the need to create dozens of individual models in Abaqus which can be very times consuming and subject to errors.

When the Python script runs through Abaqus, an input file, '<file name>.inp' is created and this file contains the information pertaining to the model in a format that is compatible with the Monte Carlo code. The Abaqus .inp file then needs to be accessible by the MCNP code in order for it to 'find' the model, therefore, communication between the two files (the Abaqus .inp and MCNP .inp) must be established. How this is done is described in the *Methods* component of this paper. MCNP6.2 is written in Fortran and requires a strict syntax in the input scripts in order for the program to operate without error. The Monte Carlo input file is built with a series of cards that each describe sections of the model. Each section of the Monte Carlo .inp file is separated by a delimiter (a blank line) that indicates when a new data card section is beginning. The general structure of a Monte Carlo .inp file is: One line problem title card (required) followed by the cell cards, then a blank line delimiter, then the surface cards followed by a blank line

delimiter, then data cards that contain information such as material composition and source definitions, then another blank line delimiter followed by anything else.

Monte Carlo cards can handle several different scenarios and the data card section provides the user with flexibility. In the data card section, the user is motivated to define the several conditions applicable to the problem they are trying to solve. It is also in this section where the user defines mesh cards for geometries that involve mesh phantoms. Unstructured meshes are embedded into the Monte Carlo .inp file in a hybrid arrangement. Since the mesh geometry is provided by the Abaqus input file, pseudo cells must be defined in Monte Carlo as a place holder so that the code can run without error. The Monte Carlo 6.2 Manual[85] provides information on the different data cards that are applicable to mesh phantom implementation including information on the necessary inputs and relevant keywords. The data cards are also where the source and source specifications are created. This includes specifying what type of source is in the model, the direction and angle of the source, as well as the mobility of the source. Since tomosynthesis uses a gantry, the source in this simulation moves along a circular path, therefore, several data cards were utilized to create the source.

To replicate a tomosynthesis system, information about the equipment settings and technical aspects is important. Therefore, the system description of a Hologic Selenia DBT (digital breast tomosynthesis) system[86] was reviewed and used as a guidance to simulate the DBT system in the Monte Carlo script. To simulate the breast model, the resources discussed in the literature review were used to replicate the relevant tissues and structures that are present in breasts. The initial basic model doesn't need every detail that exists in real breasts and only requires enough detail to prove that the simulated system works properly. The initial project stage is primarily exploratory and seeks to find the necessary data cards and the rudimentary Abaqus model that suffices an initial tomosynthesis simulation. As the project progresses, more resources will be drawn into the project to increase the accuracy and intricacy of a real breast undergoing tomosynthesis. This includes evaluating real empirical data on breast composition and structure. The accuracy of the model becomes more relevant as the project progresses therefore requiring

more resources as time goes on. For now, the resources used to build the model are outlined in the **Literature Review**.

3.2 Methods

The workflow between the different software in this project was as follows: A Python script was written in Atom.io that created an Abaqus-compatible model with mesh finite elements. Abaqus was provided the Python script and an Abaqus input file was generated. This file was then referenced in the MCNP6.2 script that was also written in Atom.io and the resulting MCNP6.2 input file was provided into the MCNP6.2 code in the terminal. This then generated an MCNP results file. The proper data cards needed to be provided into the MCNP input file to generate a file with format compatible to Abaqus software. To plot the radiograph results with MCNP, the proper data cards need to be indicated as well and if applicable, terminal commands need to be included so that the visualization with MCNP follows soon after the MCNP input file is provided into the terminal. After the Abaqus file was created, the Abaqus-compatible output file could also be opened and visualized and/or analyzed in Abaqus. For now, Abaqus input files are the only files that can be embedded into the MCNP input files through embedding with hybrid geometries. While models can be built with other modeling CAE software and converted into Abaqus-type files, this is not recommended since files created this way tend to be error prone. According to the MCNP manual, the translation from other CAE software to Abaqus raises some issues when the file is referenced into the MCNP6 input script.

As mentioned earlier, the Abaqus model can be built with a Python script. With Python, the Abaqus functions can be called while creating the model. With Python, a part(s), which is the smallest geometric tool created with Abaqus, is defined. A series of parts are created and joined into an assembly. The intricacy of the model increases with the number of parts and the user has to define the relationship that the parts have with one another. Once the structure has been defined for the various parts in the model, Abaqus can be instructed to convert the solids into a mesh. When the solids in the model are converted into a mesh, the elements that make up each mesh cell are grouped into 'elsets' or elemental sets. This strategy allows certain

properties, such as materials to be provided along with the mesh. The 'elsets' created from the meshing component in the Abaqus input files defines the pseudo cells that compose the cell card section of the MCNP input file.[87]

In the Abaqus input file generated, the *Part keywork indicates the start of the information for a given part and each part in the model is given a name that begins after the keywork 'name='. The nodes in each part are included in thee '*Part' block and the naming convention, '*Node' signifies the beginning of the node data specific to the part. The x,y,z coordinates are provided along with the node number. The '*Part' block also contains the '*Element' keyword and it marks the beginning of the element connectivity data. There are six different type of elements available in Abaqus and each has its own Element Type Code, as shown in **Table 2** below:[88]

Table 2: Table containing the different elemental codes that represent the element types. The last integer represents the total number of nodes that each element type contains.

Element Type Codes	
First-Order Tetrahedral	C3D4
First-Order Pentahedral	C3D6
First-Order Hexahedral	C3D8
Second-Order Tetrahedral	C3D10
Second-Order Pentahedral	C3D15
Second-Order Hexahedral	C3D20

Since the Python code was given element code C3D4, the element type in the model was a first-order tetrahedral. This element type has the least number of nodes and has the fastest run time. The '*Elset' keyword indicates the beginning of the elset data, and this essentially allows for the grouping of element so that various properties can be assigned to each grouping

The Abaqus input file contains the elsets tagged with a name. The elset naming format is as follows:

$$????AAAA????\_ZZZ$$

where the quadruple A represent either 'material,' 'statistics,' 'tally,' or 'source' and the triple Z at the end represent the set number, which should be unique. This format is accessible by the unstructured mesh library in MCNP6.2. In order to achieve the best results, it is recommended that this unique set number match the same MCNP number on the material cards. The elset format needs to be correct because MCNP will use the information to internally construct the appropriate elset for its use. The mesh material, which is required, contains identifying names that are independently created and are placed near the end of the Abaqus input file. The triple Z, which is unique to each material, should be a valid MCNP6 material number. To make sure that the material numbers are written correctly, the pseudo-cell cross reference table that is written into the MCNP6 output file after the REGL processes the mesh description, should be reviewed; this is where the global tracking numbers are located and describe how the pseudo cells should be specified. If necessary, Abaqus also allows for the specification of material properties. This information is simply added to the input file and used when a separate program, *um_pre_op* (which is used pre-MCNP operation), generates the MCNP6 input deck. The 'statistics' or 'tally' elsets cannot both be present in an Abaqus file and only one may be present to describe the elset. Another Abaqus file requirement is that only 1 material is allowed to describe a cell through the pseudo cells. When all components of the part have been defined, the '*Part' keyword marks the end of the part block.

The Abaqus input file also contains the '*Assembly' keyword that indicates that all the parts have been constructed. This section contains all the important information that the unstructured mesh library needs to construct the mesh from the parts. The instance block, which lies inside the assembly block, contains the number of parts that were instantiated into the assembly. The second to last keyword of interest that goes into the Abaqus input file is the '*Material' keyword where the only parameter is the material name, and this is where the unstructured mesh library retrieves it from. Lastly, the '*Density' keyword is where the user-specified density lies. As mentioned earlier, The MCNP input file is built using a series of cards, some required, some optional. This project contained multiple components: the source, the mesh

phantom of the breast, and the detector system. The three different systems could have been incorporated into a single MCNP6 input file, or they could have been placed into separate MCNP6 files and referenced inside a different 'uniting' MCNP input file. Since this project covered only the basic model (a simple system that shows simulating tomosynthesis works), a single MCNP6 input file worked just fine. As the complexity of the model increases and more variables and Python functions are incorporated to create more intricate models, separate MCNP6 files should be used so that each of the three components can be modified separately. For now, it was convenient to keep all three components on the same script so that it was easier to analyze how the three components affected one another. In addition, this method facilitated debugging since there was no need to sift through different scripts to find the source of an error.

The cell and surface cards are mandatory while the choice of data cards is optional. The cell and surface cards are responsible for setting up the geometry of the model, such as the location of the three components. For the breast mesh phantom, the geometry was built with Abaqus and referenced as pseudo cells. The source geometry was created with the cell and surface cards and the detector system was also created with the cell and surface cards. The surfaces that define the structure of the cells in the cell cards can be built using a series of equations that are defined using a keyword and the accompanying parameter entries. For example, a spherical surface would be given an 's' keyword and then provided with an x, y, x, and R entry to provide the parameters to the general sphere equation. There are numerous keywords available to build different kinds of surfaces and there are also 'macrobody' options available to facilitate surface building. Each surface is assigned a surface number and this number is used to reference that surface in the cell cards. The cells are constructed by indicating their placement in reference to the surfaces. A '-' before the surface number indicates the cell is enclosed by that surface and a positive value indicates the cell lies outside the surface. Several surfaces can enclose a single cell. The data cards, which are listed after the surface cards, provide the physics for the interactions occurring in the cells. This is where the source was defined and where the mesh specifications were located in. Data cards are used to specify the materials, the variance reduction, and several geometry specifications, such as cell volume, surface area, coordinate transformations, and several others. The first component of the model involved using data cards to specify

the source, which was the 32-keV x-ray beam, pointing in the negative-z direction and originating in the positive z-axis, offset towards the positive x-axis.

The initial model incorporated the rudimentary elements in a tomosynthesis scan and has yet to incorporate the several components behind a realistic scan. For the source creation, the MCNP script incorporated the x-ray source as a rotating source but did not include scattering and beam hardening artifacts. The source creation required two main data cards: a source specification card and a transformation card that specified the varying location of the source. The source specification card specified the type of radiation emitted from the source and other important components, such as the energy and the source strength, or flux. The transformation card specified the mobility of the source; since this was a rotating source, the transformation needed to specify the point along the rotating angle of the source. Each transformation (14 total) reflected a 1-degree shift along a 'rotation circle' where the point of origin was the bottom compression plate and the radius was the distance between this plate and the source. MCNP6 is capable of incorporating three different types of source motions with transformation cards. These are: rectilinear translation, curvilinear translation, and curvilinear rotation. Since the target remains in the same location as the source travels in a circular motion, the motion of interest is curvilinear rotation since the source's target remains towards the center of the circle.

The SDEF card has several other parameters that also needed to be specified. The 'CEL' keyword is where the source location is specified, that is, where the cell number is indicated. Otherwise, the user can specify the source location with the surface number by indicating the surface with the 'SUR' keyword. The 'ERG' keyword is also important to include since the tomosynthesis x-ray energy is about 30-40 keV (but the optimal energy is dependent on several factors), therefore, this card is needed to indicate a specific particle energy since the default MCNP6 energy setting is 14 MeV. The keyword 'PAR' is very important because this is where the particle type is specified therefore, this card is essential for letting MCNP know that this simulation includes an x-ray source and no other particle emitted from the x-ray beam. The 'TME' keyword is used to specify the time for which the source is active for. The simulation contains a moving source, and ideally, this card would be used to specify the time that it takes to collect each individual image

per angle of rotation, however, association between a rotating source and a timecard is still unclear. The keyword 'DIR' is used to specify the direction and angle of particle flight and it collaborated with the 'VEC' keyword that provided the reference vector for the 'DIR' keyword. Together, these keywords provide information on the direction and angle of the source as it moved along a 15-degree path. For this initial simulation, the source contained a cone beam geometry instead of a fan beam geometry as is typical with CT scans. The reason for this is because moving the source would require a translocation component that moves the source in an additional axis. The source would have to be translocated periodically after a given time frame. The time frame would be the amount of time taken for the source to travel along the angle of rotation. However, a digital breast tomosynthesis scan doesn't need multiple slices, therefore, a cone beam source is preferred.

Unlike the source, the breast model was stationary throughout the procedure. The model only considered the rudimentary and over simplified shape of an average breast during a scan, which was a compressed half-sphere. The assumed tumor located inside the breast was also included into the model and was given the shape of a sphere. These two components, the breast and the tumor, were given a mesh geometry and were created with Abaqus and referenced into MCNP. Their geometry was initiated in MCNP as pseudo cells, but the detail was created in Abaqus and then referenced and embedded into MCNP with data cards. The structure of the breast provided in the model was simple; a cylinder with a 6-cm height that was cut in half so that the top, it appears as a semicircle and that half-cylinder was covered by two surfaces, one on top and the other in the bottom. The tumor was a small sphere with a 1.2 cm radius and was embedded a bit off-center of the breast cell. In the cell cards, the environment outside the breast was given instructions that indicated that the breast was surrounded by a large sphere. This cell was given its own universe and the breast cells were given a different universe, since these contain a mesh universe. The following paragraphs provide detail on how MCNP6 communicates with Abaqus to create the breast cells with mesh geometry.

To establish communication between Abaqus and MCNP, the MCNP input file needs to contain an 'Embed' card section which contains all the information necessary for communication between the two

programs. To create pseudo cells in the MCNP file, the cells in the cell card section need to be assigned 0 as a surface and assigned to a universe. The universe is defined with the cell cards and encompasses everything in the geometry. The structure created with Abaqus needs to be completely enveloped within the fill cell boundary of the structure defined in MCNP. The pseudo cells in the MCNP script need to be given a null or 0 value instead of a surface card value so that the cells can be associated as normal cells while still being able to adopt features with the unstructured mesh elsets. The mesh universe that is used to define the pseudo cells can't contain any other lower universe or cells and it can't be clipped by the boundaries of the fill cell that define the universe. The 'fill cell' just means the MCNP6 cell card that contains all the 'fill' parameters of the cell and contains a collection of the defined surfaces that creates the boundaries of the defined universe. Since the pseudo cells are essentially place holders for the data provided with the Abaqus input file, all information pertaining to them in the elsets should be defined with the Abaqus/CAE tool. The unstructured mesh library in MCNP6 will use the materials and statistical information provided by the Abaqus input file to define the properties of the pseudo cells; a cross reference table is printed on the output which is accessible by the user.

It is very important to incorporate the appropriate 'calling' data cards into the MCNP code when using an Abaqus-created mesh. There is a total of eight different data cards that can be used with the unstructured mesh to establish a connection between Abaqus and MCNP and while they don't all have to be used, at least one is required. The eight options include: EMBED, EMBEE, EMBEB, EMBEM, EMBDE, EMBDF, EMBTB, and EMBTM. They each fulfill a different purpose and for his project, the EMBED and the EMBTB data cards were used. The EMBED card provided the geometry specification and the numbers on this card had to match the cell numbers in the pseudo cell cards. The information required on an EMBED data card included the background specification, which was the pseudo cell that served as the background cell, integer pairs that paired the embedded mesh pseudo cell with the MCNP pseudo-cell from the cell block, the mesh type specification (Abaqus in this case), the name of the Abaqus input file (which should be in the same directory that the MCNP code is located in), and the name of the file that contained the results. There are other additional optional entries that could have been placed inside the

EMBED card that were not relevant in this project. The other data card that was relevant for this project was the EMBTB card, which was used for time bin boundaries. This data card only required one input, which was a list containing the different time bins for the data creation. Since tomosynthesis was conducted in a series of 'slices,' the results were generated in miniscule time steps, therefore, this data card was used to specify the time bin for each separate angle used. However, this step was found to be redundant since the mesh tally used for the radiograph was also capable of receiving data at separate, user-defined, time entries.

While there was a 'source' component in the MCNP input file that represented the tomosynthesis x-ray source, there is a different source that needs to be considered at some point, which is the breast model itself. When the source interacts with the breast model, secondary particles are generated, and this contributes to scattering and noise. Although some of the scattered secondary particles escape, there are a good number of secondary particles that end up in the detector component. Therefore, the breast model needs to be considered as a source to incorporate the scattering physics that go into the image creation. The breast model has a mesh geometry, therefore, the source defined in this region needs to be treated differently than the x-ray source. The breast model is treated as a uniform source, therefore, scattering radiation that emerges as a result of x-ray interaction needs to be defined as a 'volumer' source. The position parameter in the source card for the mesh volume is then set to 'volumer' so that uniform sampling is assigned to the entire mesh region. Scattering occurring inside the breast can then be considered into the detector component of the simulation.

Abaqus-created statistical analysis is not required to analyze the results and in order to use MCNP statistical analysis, a tally, or set of tallies, should be used on the appropriate pseudo-cells. Tallies were used to simulate detection because tallies can count the number of photons that cross a given geometry given a photon flux. This is important for tracking the photon interactions occurring inside the breast during the scan as well as tracking the photons that leave the breast and enter the detector component of the model. When incident photons go into the detector in a tomosynthesis scan, the signal is vulnerable to noise and intrinsic efficiency therefore the signal received from the incident photons is not perfect. There are several

factors that need to be considered to create this realistic detector system, such as scattering within the detector elements, the effect of detector size on the signal and subsequent image quality, charge trapping, among several other effects. In their tomosynthesis detector system, Hologic uses amorphous selenium for the detector, therefore, this simulation will eventually consider this material for the detector component.[89] For the sake of simplicity, the initial simulation didn't take into consideration noise due to the electronic components and the detector was only exposed to noise due to scattering and escape of the photons incident onto the detector elements.

The detector component consisted of several pixels creating a total detector area of 233 mm x 287 mm. In the real model, the flat panel detector contains a transistor for each pixel and in the Hologic model, the pixel size is 0.07 mm, therefore, their flat panel contains a pixel area of 2560 x 3328. The pixels are representative of pixels that are in the output image. Ideally, each of these pixels should be represented by cells and the incident x-rays per cell is considered as a contribution for the overall image production. The MCNP code treats the flat panel detector as a series of energy integrating detectors where each pixel integrates the total energy received from the incident photons. Each pixel in the detector area is then a pixel in the resulting image. To count the total amount of energy that is deposited per pixel, tallies should be used to track the particles that traverse the pixel region and deposit their energy. In this model, an oversimplified model of a tomosynthesis scan was used, therefore the pixel size was 0.2cm instead of 0.07mm, but as mentioned before, the initial simulations of this project were to verify that the system works and that an image could be produced from the three components. As the model's accuracy increases, the intricate electronic components and signal loss should be considered into the model.

The MCNP6 input file needs to be provided into the terminal as long as the file is located in the same location as the program. An output file doesn't have to be specified, as MCNP6 will output one with a default name, however, it is highly recommended to specify the name of the output file so that it is easier to keep track of the file instead of looking for a file with an arbitrary name. To output the results into a format that is compatible with Abaqus, the MCNP results calculated in the mesh need to be printed on a separate output file that is converted into an .odb format. This file type can be used by Abaqus as a source

term for finite element analysis or visualization. If visualization on the detector element is needed, then the detector element needs to be created with Abaqus as well and be given a mesh geometry. For the sake of simplicity for the initial simulations, the detector interactions in the pixels were analyzed with MCNP and Python. Data cards in MCNP6 can be used to set output control so that certain file formats can be generated, however, this was not necessary for this project. MCNP has an interaction plotting tool and to use it, the MCNP output file needs to be in a format compatible for plotting with the MCPLOT plotting tool. MCNP6 can produce transmitted image projection with the radiograph tally which treats the detector grid much like photographic film. To create a rectangular radiograph, the 'FIR' card can be specified. The output created by the radiograph tally is then contained in the MCTAL file. To use this directly with the MCNP tally plotter, the 'FREE SC' command should be given on the terminal or by including the 'MPLOT' card into the MCNP6 input file. However, creating a radiograph with the 'FIR' command resulting in a time-consuming process with high memory uptake, therefore, a mesh tally was used instead to replicate a flat-panel detector. While the results could have been plotted with MCPLOT, the results were instead plotted with Python's matplotlib.pyplot instead because this plotting tool was found to be more intuitive and better at image manipulation.

4 Results

As mentioned previously, the purpose of this paper was to describe the initial stages of a project that aims to simulate a realistic tomosynthesis scan. Therefore, the results discussed in this section demonstrate the initial outcomes of the 'test runs' that will eventually be developed into a more sophisticated model. After reading the tomosynthesis standards outlined by Hologic, the model in the MCNP input file was created to replicate the tomosynthesis equipment and the scan, therefore, the results include a dissected 15-degree scan of a breast phantom and instead of rendering the multiple images of the simulated scan, each picture will be shown individually in this section. To create the plots, Python's matplotlib.pyplot function was used to recreate the mesh tallies acquired from MCNP6.2 and create contour plots similar to those created with the MCPLOT MCNP tool. The reason for this is due to the easy

customizability provided by Python's plotting tools as well as speed. MCNP's interactive plotting tool is susceptible to lag and the default color scale of the program can't be customized to favor these results.

First, the unstructured mesh of the breast phantom was created with a Python script and then generated with Abaqus. The result of this process is shown in **Figure 2** and the coordinate orientation of
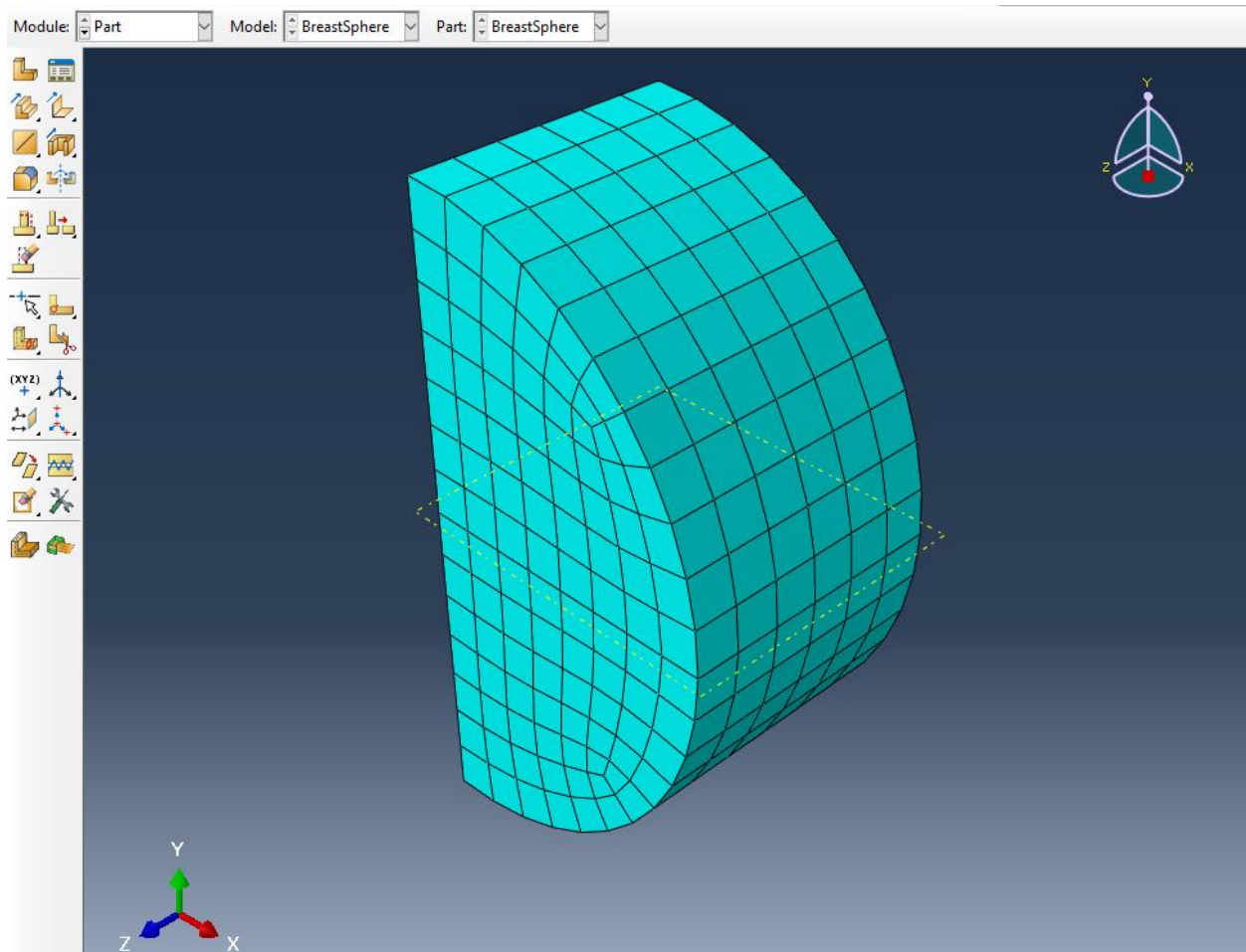
Figure 2: The mesh phantom of the breast geometry created with Abaqus. The dimensions are: height = 6cm (z-axis), and radius = 7cm (centered at the origin).

the breast model is shown in the bottom left corner. The model was created with first-order tetrahedral and the total number of nodes in this geometry is 826. Although the model is sideways, the x-ray source is programmed to be normal to the panel facing the positive z-axis. The detector panel is programmed to be a couple inches away from the opposite plane which is invisible to the viewer in **Figure 2**. In the MCNP

code, this breast mesh phantom was placed between two compression plates, therefore, the breast was 'sandwiched' between two planes. This configuration is shown in **Figure 3**. The source was located a couple
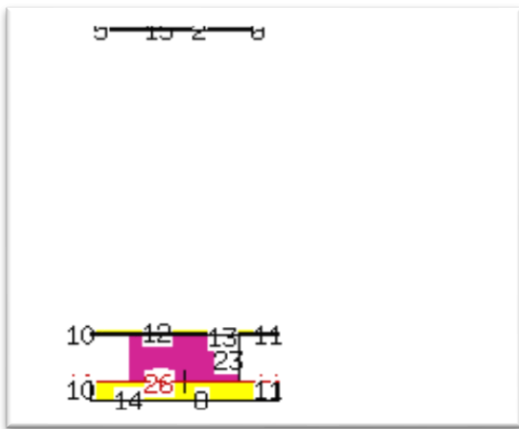
Figure 3: configuration of the geometry created with MCNP, plotted by the interactive plotting tool

of inches above the plate enclosed by surfaces 5, 6, 15, and 3 (top of the picture). The top compression plate is thin: the thickness is only a centimeter thick. The bottom compression plate is thicker by nearly a three-fold and is immediately followed by the selenium 'detector' panel. The 'center' of the tomosynthesis scan is the top of the bottom compression plate. This 'center' is the focal point for which the source rotates around and the detector plane remains exactly opposite of the source and there is no

change in proximity throughout the simulated scan. When the source is rotated, the positive direction is towards the positive x-axis and the rotation occurs with no change in the y-axis (source remains at y=0) and the negative direction is when the source moved towards the negative x-axis. To achieve the rotating source dynamic, transformation cards where created for fourteen orientations since the fifteenth position didn't require a position. Each transformation card pertains to a single degree along the 15-degree path of the rotating source. To create a 'transformation' with a transformation card, an 'origin' needed to be established to compare it to the origin of the non-transformed model. The source was not rotated about the origin, but instead, the center point of the bottom compression plate, therefore, a new origin was established for each transformation. Each position was established for the same amount of time, therefore, the number of histories for each degree was equal and no biasing was used.

The tumor embedded into the breast model was a 1.2 cm-radius sphere located at (2.5, 1, 3) and was composed of water and iodine, therefore, it was highly accentuated inside the water-based breast model. The detector panel created with mesh tallies was given a dimension of 24 cm (y-axis) by 20 cm (x-axis)

which is 9 inches short of the 24x29 panel given by Hologic but the extra five inches provided no useful

information, so they were excluded in this model for the sake of simplicity. In addition, the pixel size used
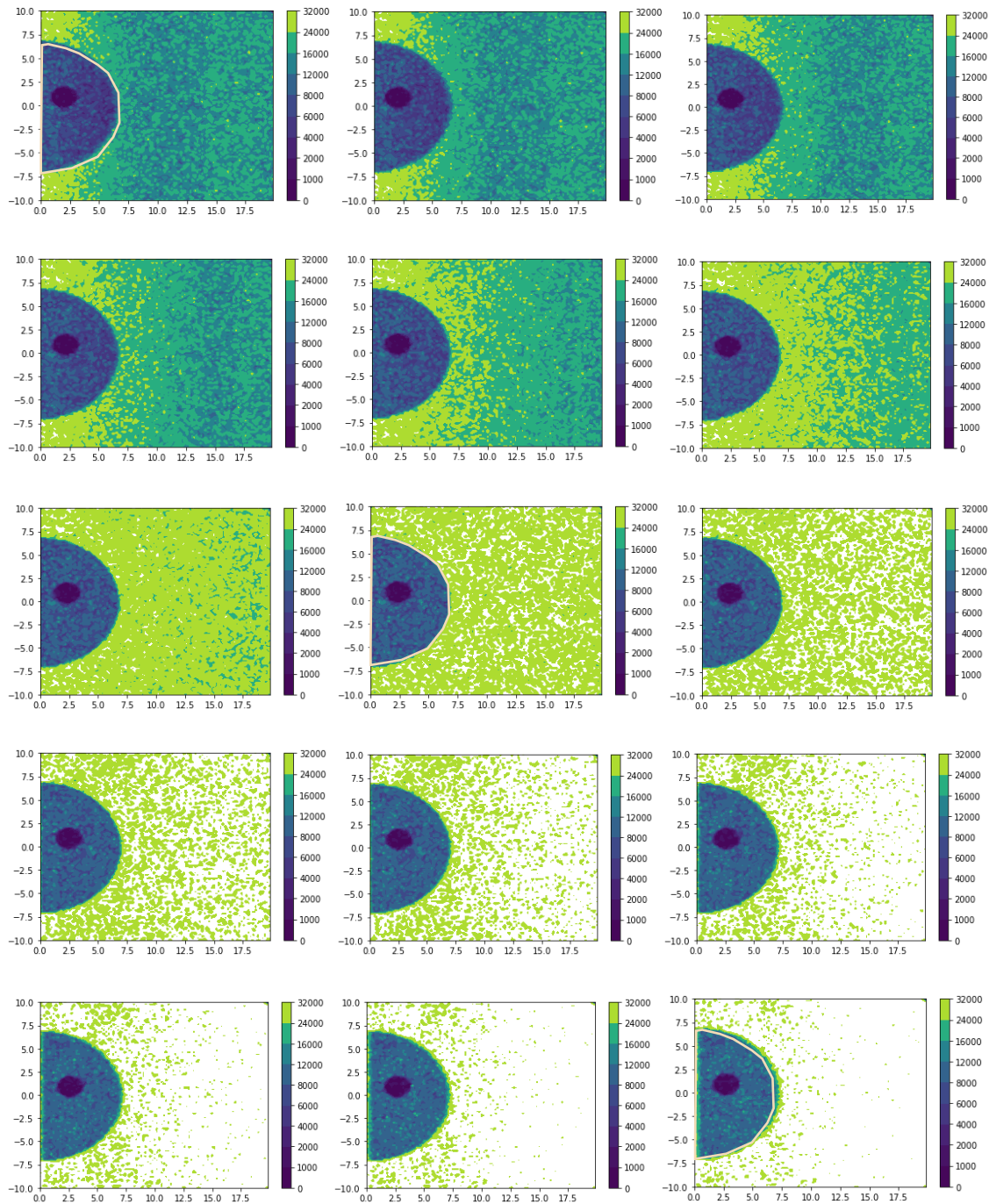
Figures 4 (a-o): Results of simulation. Each picture represents a simulated 'slice' of the tomography. The images are all taken at 1-degree intervals where (a-the top left picture) is taken at positive 7 degrees, (h-center, center) is taken at 0 degrees, and (o- bottom right picture) is taken at negative 7 degrees. A light-yellow semi-circle outlines the breast at 0 degrees to reflect the true size of the breast. This semicircle is then used to compare the true size of the breast to the breasts distorted at the various projections.

is 0.2cm by 0.2 cm which is ten times by ten times larger than the Hologic pixel size but since this was a simple model with no fine detail, a fine resolution wasn't needed. The resulting images of this detector plane combined with the geometry are shown in **Figures 4a-o**. The graphs (developed with Python), contain a color scale on the right side of the image and this scale can be used to estimate the flux throughout the image. A dark color is associated with a low flux and a bright, green or yellow color is associated with a high flux. As the source rotated along the multiple degrees, the shape of the breast became slightly distorted. The distortion is barely noticeable, therefore, a thin yellow outline of the original shape of the breast (0-degrees) was placed on the first and last images to demonstrate the truncation and elongation at the positive and negative 7 degrees respectively. The background (area that is not the breast), is shown to increase in brightness along the multiple images and eventually, this feature should be eliminated so that the viewer can focus solely on the anatomy of the imaged breast.

The tumor was accentuated in each figure as a dark circle close to the center of the breast. The flux was very low in this region as indicated by the color scale and this is probably due to the high content of iodine. The results demonstrated an idealistic contrast between the breast and the tumor, however, in a more advanced and realistic model, this contrast will not be as high because the iodine contrast (or some other contrast agent) will be lowered to reflect realistic conditions. In addition, the color scale will be adjusted to favor low fluxes so that regions with higher density can be better differentiated. In these results, the background flux is too bright because there is little to no attenuation compared to the breast and the tumor, however, the color scale needs to be adjusted to reflect the zero importance of the background.

5 Discussion

This following section discusses the results and the associated challenges of obtaining the results that were encountered along the way. Interpretation of the results is provided and more detail on how results were acquired that is not found in the **Methods** section is given in this section. The results obtained from this project provide evidence of the feasibility for further development of the project. Hence, this section

also contains discussion on the future prospects of the project that describe how the model will be further developed.

5.1 Discussion of the Results

The results demonstrate a promising future for this project. The images shown in **Figures 4a-o** show an accurate representation of the geometry provided in the MCNP code and the tumor, which was given iodine contrast, is clearly visible in all fifteen projections. In addition, the slight shift in rotation degree is reflected slightly in the elongation or truncation of the original breast geometry. This provides assurance in the transformation cards; the best way to see if the transformation cards are working properly is to plot the results of the multiple shifts. The results also demonstrate significant attenuation compared to the background. The difference in flux between the breast model and the background, which can be quantified with the 'Viridis' color scale provided on the right of each graph, demonstrates appropriate absorption in the breast region.

In this model, the resolution is relatively poor: 0.2cm x 0.2cm, therefore, the results appear a bit grainy. The reasons why a finer resolution as not used is because a) the simplistic model didn't need a fine resolution, b) creating this simulation required a lot of de-bugging, therefore, the simulations were made simple and not as time consuming. Improving the resolution by a 100-fold will significantly increase run time which is still acceptable for a fine-tuned model, but again, that was not a necessary step for this simulation. As the model increases in complexity, finer details such as millimeter-sized vessels, will have to be visualized to reflect a realistic tomography scan, therefore, a fine resolution will be necessary. A finer resolution will also help visualize slight shifts in density better, which was not necessary in this scan because only a single dense object was embedded into the tumor. The simulated model needs to be able to detect density shifts as low as 1 Hounsfield Unit difference, therefore, this requirement is important to implement into the model to maintain the integrity of the simulated system.

A noticeable feature of the 15 resulting images of the tomosynthesis scan is the inadequate color scale. As mentioned earlier, the scale is linear and does not cater to areas of low flux. In order to ensure

that 1 Hounsfield Unit differences in the model are noticeable, the color scale needs to be adjusted so that the difference in attenuation between the fatty breast tissue and the background isn't as exaggerated and the differences between the anatomical breast components are more easily differentiated. An easy solution would be to completely remove the background; however, this would require adjustment for each different breast scanned since the size of the breast affects the visible background. Instead, the color scale should be adjusted to have a cut-off flux so that flux slightly above the flux of the fatty components of the breasts are treated equal, or at least close to equal. Fatty tissue is the least dense component of the breast, therefore, the flux that results from fatty regions is the 'maximum' flux seen from the breast. Treating this flux as breast cut-off flux can help refocus the color scale to cater to higher densities which will help differentiate slight shifts better. The problem is that resulting flux (flux that hits the detector panel), is dependent on breast thickness, since larger breasts with higher thickness will have more absorption, therefore causing an overall decrease in resulting flux, even if the source flux remains the same. To fix this problem, several different thicknesses can be experimented with to acquire a rough estimate of the flux seen from the multiple breasts and compare this with the background. It's predicted that no matter what thickness of breast is used, the background flux striking the detector will remain the same and the difference between the thinnest breasts and the background will still be large enough to establish a cut-off between breast flux and background flux. In other words, the flux observed through thinner breasts can be used as a cut-off to treat the background flux not much different from the flux through fatty tissue so that the color scale is re-centered to better differentiate the multiple components observed in the breast.

In the results shown in **Figure 4 (a-o)**, the spherical tumor doesn't appear to distort throughout the projections the same way that the breast model does, and this is because of the symmetrical properties of the tumor. In reality, tumors are not perfect spheres and they can take on many different shapes with no symmetry. This means that the tumor size and shape might appear different at multiple angles. The extent of the tumor distortion has yet to be defined, however, severe distortion from one projection to the next can indicate the extent of the asymmetry of the tumor and can also provide some indication of the dimensions of the tumor. For example, if the tumor has a cylindrical shape facing upward (height is on the z-axis and

radius extents on the x-y plane, then from the 0-degree scan, the tumor will appear as a sphere, however, if the source and detector panel are rotated 7 degrees to the negative or positive direction, then the height of the cylinder becomes more obvious and it becomes clear that the tumor does not have a spherical shape. Hence, exploring the effect of rotation angle on the visibility of the tumor shape and size is an important task.

The detector panel can 'see' the breast up to the chest wall at which point the region surrounding the chest wall is invisible to the detector plane. The area leading up to the chest wall is susceptible to artifacts, as seen in the fifteen projections. When the rotating source is shifted towards the negative x-axis, the visibility of the area close to the chest wall decreases. This problem can be fixed by changing the axis of rotation so that instead of having the source travel along the x-axis, the source can travel along the y-axis. Other artifacts will also be explored further as the model's intricacy increases. A major artifact to account for is the streak artifacts which commonly occur in imaging scans of dense objects, such as metal or bone.[90] Although there is are no bones in breasts, certain contrast agents might cause streak artifacts, depending on their concentration and their effective-Z value. There are no streak effects visible in the iodinated tumor and typically, mammography images don't contain streak artifacts in them. However, perhaps incorporating gold particles in the breast might change this in which case measures will be taken to correct for the streaks. A technique to correct for streak artifacts is to increase the voltage so that higher energy x-rays, however, this might cause a reduction in the tissue contrast. This trade-off will be worth exploring if streak artifacts become visible as more components are added to the model.

As the intricacy of the model increases and the accuracy of the tomosynthesis equipment begins to resemble that of a realistic machine, more components will be incorporated, including the cathode and anode pieces that create the x-ray beam in a real tomosynthesis machine. Although the source is simulated with the MCNP input file, the components can still be mapped onto the model to make the source as realistic as possible. This means that particle interactions with the surrounding metallic components will play an impact on noise and other consequences, such as the heel effect. The heel effect, shown in **Figure 5**, occurs
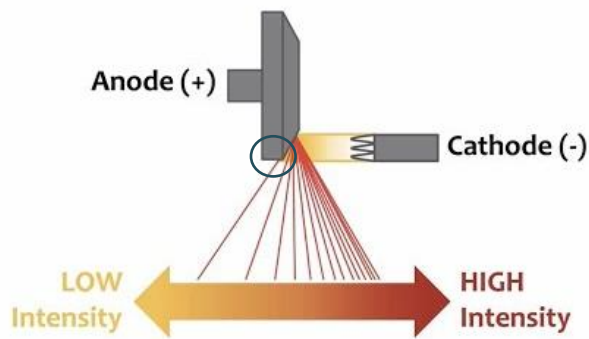
Figure 5: Graphical representation of the heel effect. The 'heel' is circled in the image.[91]

when the anode heel (which is highlighted in the image with a circle) absorbs some of the x-rays that results from the anode-cathode interaction, therefore causing a reduction in intensity in that region thus resulting in an uneven x-ray intensity throughout the scan. There is an inverse relationship between the angle of the anode

and the anode heel effect, therefore, to reduce the effect of the anode heel, the anode angle can be increased for a more even distribution of the beam intensity. Another way to reduce the anode heel effect is to increase the distance between the source and the target so that the beam distribution levels out better as the beam reaches the target. In addition, broadening the beam to better suit a large field size can reduce the heel effect but since the breast is relatively small, the broad beam will simply have to be collimated around the edges of the equipment to reduce the amount of radiation outside the target region therefore reducing dose to the patient.

There are three main methods to create a radiography with MCNP. The first method is to use a FIR card, which is essentially a tally card designed to create a radiograph of a rectangular panel. This card detects either the flux of the incoming particles in particles/cm^2 or energy deposition per unit area with units of MeV/cm^2. This method utilizes a 2D plane and the card itself contains 10 input parameters, including a parameter that allows the user to specify if they would like to include scattered photons along with direct source photons or only one or the other. This method is the simplest of the three and perhaps the most self-explanatory. The second method is to establish a tally mesh with the TMESH card and specify a rectangular plane with RMESH. Unlike the FIR tally, this method is 3D with a mesh that contains a height parameter as well. The lattice tally works similarly to that of a mesh tally but can results in faster run times. They are constructed from a 'repeated structure' provided by the user. In the manual, MCNP6.2 doesn't go into detail

on the application of lattice tallies except that they are also capable of producing contour plots. This model uses a mesh tally because of its robustness and close resemblance to that of a realistic detector panel. It can be rotated and can be provided with tally modifier cards. It is unclear at the moment if it can be provided with a tally modifier that instructs the tally to follow a certain response function, but it can be provided with energy cards, timecards, and cosine cards.

Using the mesh tally method is more accurate to a realistic detector because the height of the mesh can match the height of the selenium in the detector. The RMESH can then return the results of the photons that deposited energy into the detector element and the photons that escaped the mesh element don't have to be counted. With an RMESH, a set of planes are given in the x, y, and z axis to create a grid containing multiple mesh elements. These elements can be sized to resemble pixels which was done in this model. The RMESH was also provided with transformation cards to mimic the rotation of the source, this way, the detector mesh was always normal to the source beam. There are four different types of mesh tallies: type 1 is a track-average mesh tally (which was used for this model), type 2 is a source-mesh tally, type 3 is an energy-deposition mesh tally, and type 4 is a DXTRAN mesh tally. Mesh tallies can be provided with response function cards (MSHMF), however, the MCNP6.2 manual does not provide a list of the different response functions that can be provided nor is there any specification on how to denote the different response functions. The ERHSG card is a card that references tally modifier cards En or Tn, that specify the energy bins (in MeV) or time bins (in shakes) for which the tally should detect. Unlike the FIR card, the mesh tally card doesn't have an input parameter that can ignore scattered photons.

To reduce noise from scattered photons, the model can be provided with a collimator, or the tally can be provided with a cosine card. The model shown in the results uses an energy modifier card to instruct MCNP to ignore photons that are not equivalent to the source energy. Energy less than the source energy implies a scattered photon; therefore, these were rejected. Modeling a collimator would reduce the scatter but would also reduce the sensitivity since photons are susceptible to absorption in the collimator material. Another method would be to implement a theoretical collimator with infinitely thin walls by using a cosine card that ignores photons that do not strike the detector panel at a 90 degree or close to 90-degree angle.

Photons with an angle that isn't close to a 90-degree angle implies the photon was scattered and ignoring it would help reduce noise.

A challenge encountered with the model was the implementation of a timed rotation. An ideal model would be one that is given a single rotation card that extends from 7 degrees to negative 7 degrees and makes a 'stop' at each degree so that an image can be acquired. However, there is no MCNP6.2 card provided by Los Alamos that associates a rotation with a timed response. The MCNP input script can be provided with a tally timecard that acquires tallies at multiple time intervals but unfortunately, the tally timecard and the transformation card cannot be associated so that a position along the rotation pertains to a specific time stamp. In addition, MCNP does not have functions like other programming languages that can provide results based on a set of given conditions. A for-loop filled with if-statements would help associate the rotation with time but alas this is not a functionality capable with MCNP. Instead, the MCNP script was provided with 14 transformation cards, each belonging to a 1-degree rotation along the rotation path. The 0-degree position didn't need a transformation card. The cards were swapped out one at a time and tally results were generated individually as each the script was re-run 15 times in the terminal and the tally files saved as different names.

Instead of running the script 15 times to acquire a tally at each angle, the source can be given a set of transformation cards:

Source: TRi <transformation parameters>

     TRj <transformation parameters>

     --- inside the SDEF card---

     TR= dn

     ----

     dn TRi TRj

However, the mesh tally detector can only be given one transformation card at a time. A solution would be to create a source with multiple transformations, as shown above, and the detector plane can be given a

cosine tally modifier card that contains 15 cosine bins where each cosine bin is normal to (directly faces) one of the 15 source positions. This method would cause elongation of the detected image since a detector plane that is not normal to the incident beam and instead, at an angle from the source, would cause 'stretching' of the signal. A graphical representation of the 'stretching' is shown in **Figure 6**. An angled source causes distortion in the image, therefore, an algorithm would have to be used so that the stretching can be reverted. Unlike the graphical representation of the distortion shown in **Figure 6**, the distortion won't be as severe since the maximum angle away from the origin is only seven degrees. However, the elongation should not be ignored to retain the model's
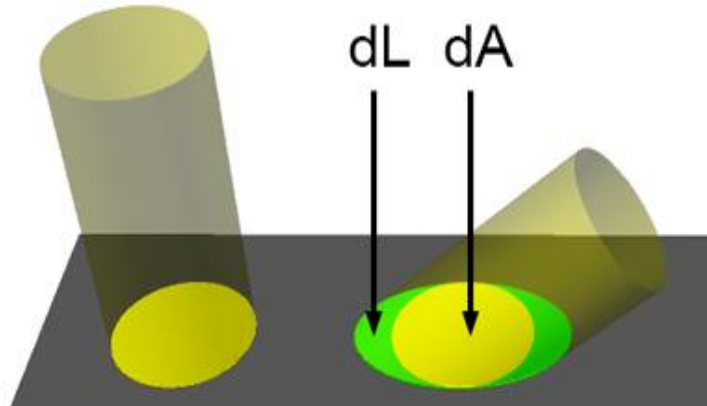
Figure 6[92]: A graphical representation of the distortion that occurs in the image due to an angled beam.

accuracy. Providing the source with a set of transformations instead of providing each one one-at-a-time saves time and effort. Time gating the rotation is still not possible, at least not with an intuitive method, but providing the source with the set of transformations guarantees that each position along the rotation path is imaged for an equal amount of time. If the bias and probability are set equally for each of the fifteen transformations.

5.2 Future Prospects

The work done in this project is for the purpose of a larger-scale simulation project. This simulation provides the backbone to a project that will simulate several varieties of breast cancer and breast type. This 'large-scale' project's purpose is to investigate the efficacy of different contrast agents without requiring expensive and time-consuming human trials that might not provide enough variety to confirm if a contrast agent truly works. Because the simulations must essentially provide a substitute for real tumor-containing

breasts, the breast model and the tomosynthesis simulation have to be as accurate as possible. This means creating a model that considers the biophysics as well as radiation physics that take place during a breast imaging scan. The model created in this project is very basic in comparison to what the model will become in the future; the goal is to incorporate every detail as computationally possible, including the vasculature and the sub-centimeter details of the breast structure as well as the material composition and how it varies throughout the breast. In future developments, motion will be incorporated into the model, such as circulation and other physiological processes. Computed-tomography systems have the ability to detect materials apart that are at least 1 HU different and so it is important for the simulation to take into account the slight shifts in density inside the breast tissue. While several anthropomorphic models have used water to represent tissue, the final model will incorporate the differences in tissue composition for each component of the breast because this is what helps create the density differences.

Creating a realistic model means incorporating the biokinetics that contrast agents depend on; this means incorporating the half-life of the contrast agent, its affinity to certain types of tissues, its osmolality and viscosity, and particle size. The half-life of the contrast agent helps determine the circulation time of the contrast agent before it's removed by the body. This helps determine an approximate concentration of the contrast fluid at the time of the imaging scan. The affinity to tissues is dependent on the contrast molecule and any antigens it may contain. If it contains tumor-specific antigens, then the concentration will be a certain factor higher in the tumor than in the surrounding tissue. If the tumor-targeting antigen is injected into a patient that contains a tumor that is not compatible with the antigen, then the contrast agent will not be effect and this, of course, will be incorporated into the simulation code. The osmolality, particle size, and viscosity help determine its ability to travel from the vasculature into the tissue. Smaller particles are more readily absorbed in permeable vascularization that surrounds tumors compared to larger particles. Other contrast agent properties that are not biokinetic related are also important to the simulation, such as particle density – which influences the contrast to noise ratio between the target versus non-target tissues – and elemental components – which help determine the effective-k value that plays an important role in x-ray absorption.

The biophysics will be 'simulated' with a Python script that outputs Abaqus-ready scripts based on inputs provided by the user. The inputs will be a contrast agent type (a string character from a predefined library of contrast agents), time between injection of the contrast agent and the time of scan (in seconds), size of the breast, breast density (1 out of the 4 BI-RADS type), tumor type, and tumor size or stage. These inputs will be used to create the different breast components such as the tumor, vasculature, lobules, etc., that will each be created as an individual part in Abaqus. The contrast agents will have varying materials with different properties so that resulting Abaqus files will have material cards that are dependent on the contrast agent of choice. The presence of contrast particles in the target region are dependent on the time frame, therefore, it is important to factor in the time that passes between the injection and the scan. The time then provides the user with an Abaqus model that is reflective of the contrast agent distribution during the given time frame. The Abaqus files generated from this Python code are then used to create Abaqus .inp files that will be used in the MCNP EMBED cards.

The MCNP6.2 script will also be generated with Python for a couple of reasons. First, The MCNP simulation will also contain user-specified variables, such as x-ray energy, angular distribution of the x-ray, scan time, and distance from the source. Secondly, the MCNP geometry is dependent on the Abaqus geometry and the amount of Abaqus parts affect the amount of pseudo cells in the MCNP model. Therefore, the MCNP scripts should be automated with a Python code. While most of the geometry in the MCNP code will remain the same, the Python code will be able to generate some variability based on user inputs such as, the source energy and flux, source angle of rotation, breast height (distance between compression plates), and Abaqus inp. files. Python will read the Abaqus .inp files to write the pseudo cells on the MCNP scripts and the material cards. The materials on the Abaqus files need to match the material cards on the MCNP script, therefore Python will reiterate the materials from the Abaqus files into the MCNP script.

The MCNP script will then run on the terminal and will generate output files based on the instructed output files. This MCNP script generates radiographies based on the inputs provided by the user, therefore, a radiography is expected to be plotted using the MCNP PLOTTER tools with the results gathered from the detector tallies, or, Python's matplotlib functionalities. The radiographs will be used to find the efficacy of

different contrast agents and to see what the limits of detectability are for various factors, such as tumor size, tumor position, and metastasis. To ensure that the most accurate models are used, future prospects of the project involve communication with OHSU to receive guidance on the imaging procedure as well as breast anatomy. OHSU can also provide assistantship on amorphous selenium detectors or other flat panel detectors used for breast imaging so that their functionality can be properly incorporated into the simulations. As mentioned, the broad goal of the project is to provide a 'testing' system where different contrast agents are experimented with on an accurate model to avoid long and expensive human trials before knowing if a contrast agent is efficient or even viable. The project will ultimately offer an exploration tool for different contrast agents and imaging settings that can aid in the visibility of non-obvious tumors, like those in dense breasts or the ones located in obscure regions.

6 Conclusion

The results demonstrate promise and prove feasibility for the second stage of this project. The results proved reliability in the methods used to create the simulation and also showed that MCNP can replicate physics accurately as long as the input files contains the correct cards and the correct geometry. The input cards used in this project were sufficient for this simplistic model, however, as the model's complexity increases and several components are expected to be integrated into the model, new data cards will be used and parallelization will become increasingly important at storage and memory requirements are increased. Creating this model required several checkpoints and continuous quality-checks to make sure that MCNP wasn't producing any errors and that the generated results were accurate. A simple model was important in this first stage project because using a simple model makes it easier to know if MCNP is not producing the correct results and if the model is not being read correctly from the input script by the program. This was especially important when creating the rotating source and the 'detector' with the mesh tally. A trial-and-error approach would have been more difficult with a complex model because the results would have been more ambiguous and the source of error would have been harder to identify.

Now that a simulation has been created and the results produced from this simulation are accurate, the multiple components of a real breast will be incorporated into the mesh phantom. The detector will also be further developed to mimic a real tomosynthesis detector. This includes increasing the resolution, incorporating detector noise that is experienced with amorphous selenium, factors that decrease the sensitivity, and other sources of electronic noise. The overall environment will also be further developed so that the many aspects that affect a tomosynthesis scan can be incorporated and their effect on the results can be analyzed. This includes equipment noise, the heel-effect, and other artefacts. Finally, multiple contrast agents will be incorporated into the breast model and the biophysics will be incorporated so that the contrast agent performance and efficacy can be accurately measured. There is still a long way ahead to create a model that can be used for theoretical calculations, but the promising results shown in this paper provide one step closer to achieving that model.

7 References

[1] Digital Mammography - Mammography - Imaginis - The Women's Health & Wellness Resource Network". www.imaginis.com. Archived from the original on 30 January 2012. Retrieved 4 May 2018.

[2] Bcnapinklady. "Mammographic Density and Screening." Breast Health and Awareness - Breast Cancer Network Australia, www.bcna.org.au/breast-health-awareness/mammographic-density-and-screening/.

[3] "Breast Density." *Breast Density*, www.bccancer.bc.ca/screening/breast/breast-health/breast-density.

[4] "CT Scan (CAT Scan, Computerized Tomography) Imaging Procedure". MedicineNet. Retrieved 2018-11-29.

[5] Ha, Alice; Lee, Amie; Hippe, Daniel; Chou, Shinn-Huey; Chew, Felix (July 2015). "Digital Tomosynthesis to Evaluate Fracture Healing: Prospective Comparison With Radiography and CT". American Journal of Roentgenology. 205 (1): 136–141. doi:10.2214/AJR.14.13833. PMID 26102392

[6] Peplow, Douglas E., and Kuruvilla Verghese. "Digital mammography image simulation using Monte Carlo." *Medical physics* 27.3 (2000): 568-579.

[7] Dance, D. R., et al. "Breast dosimetry using high-resolution voxel phantoms." Radiation protection dosimetry 114.1-3 (2005): 359-363.

[8] Fedon, Christian, Marco Caballo, and Ioannis Sechopoulos. "Internal breast dosimetry in mammography: Monte Carlo validation in homogeneous and anthropomorphic breast phantoms with a clinical mammography system." Medical physics 45.8 (2018): 3950-3961.

[9] *Proceedings: Monte Carlo Modeling of Mammographic Images*, web.ornl.gov/~peplowde/p008.html.

[10] World Cancer Report 2014. World Health Organization. 2014. pp. Chapter 1.1. ISBN 978-92-832-0429-9.

[11] Bray F, Ferlay J, Soerjomataram I, Siegel RL, Torre LA, Jemal A (November 2018). "Global cancer statistics 2018: GLOBOCAN estimates of incidence and mortality worldwide for 36 cancers in 185 countries". Ca. 68 (6): 394–424. doi:10.3322/caac.21492. PMID 30207593.

[12] "Breast Cancer Treatment (PDQ®)". NCI. 23 May 2014. Archived from the original on 5 July 2014. Retrieved 29 June 2014. World Cancer Report 2014. World Health Organization. 2014. pp. Chapter 5.2. ISBN 978-92-832-0429

[13] Paine, Ingrid S.; Lewis, Michael T. (2017). "The Terminal End Bud: the Little Engine that Could". Journal of Mammary Gland Biology and Neoplasia. 22 (2): 93–108. doi:10.1007/s10911-017-9372-0. ISSN 1083-3021

[14] Susan Blackburn (14 April 2014). Maternal, Fetal, & Neonatal Physiology. Elsevier Health Sciences. pp. 146–. ISBN 978-0-323-29296-2.

[15] Macéa, José Rafael; Fregnani, José Humberto Tavares Guerreiro (1 December 2006). "Anatomy of the Thoracic Wall, Axilla and Breast" (PDF). International Journal of Morphology. 24 (4). doi:10.4067/S0717-95022006000500030.

[16] Birbrair A, Zhang T, Wang ZM, Messi ML, Enikolopov GN, Mintz A, Delbono O (August 2013). "Role of pericytes in skeletal muscle regeneration and fat accumulation". Stem Cells and Development. 22 (16): 2298–314. doi:10.1089/scd.2012.0647. PMC 3730538. PMID 23517218.

[17] Ghosh, K., Brandt, K.R., Reynolds, C. et al. Tissue composition of mammographically dense and non-dense breast tissue. Breast Cancer Res Treat 131, 267–275 (2012). https://doi.org/10.1007/s10549-011-1727-4

[18] "Breast Cancer Treatment (PDQ®)". NCI. 23 May 2014. Archived from the original on 5 July 2014. Retrieved 29 June 2014. World Cancer Report 2014. World Health Organization. 2014. pp. Chapter 5.2. ISBN 978-92-832-0429

[19] World Cancer Report 2014. World Health Organization. 2014. pp. Chapter 1.1. ISBN 978-92-832-0429-9.

[20] Masood, Shahla. "Breast cancer subtypes: morphologic and biologic characterization." Women's Health 12.1 (2016): 103-119.

[21] "Molecular Subtypes of Breast Cancer." Breastcancer.org, 21 Jan. 2020, www.breastcancer.org/symptoms/types/molecular-subtypes.

[22] Perou C, Sorlie T, Eisen M et al. Molecular portraits of human breast tumors. Nature 406(6797), 747–752 (2000).

[23] Adrada B, Arribas E, Gilcrease M, Yang WT. Invasive micropapillary carcinoma of the breast: mammographic, sonographic, and MRI features. Am. J. Roentgenol. 193, W58–W63 (2009).

[24] Lacroix-Triki M, Suarez PH, MacKay A et al. Mucinous carcinoma of the breast is genomically distinct from invasive ductal carcinomas of no special type. J. Pathol. 222, 282–298 (2010).

[25] Winchester DJ, Sahin AA, Tucker SL, Singletary SE. Tubular carcinoma of the breast. Predicting axillary nodal metastases and recurrence. Ann. Surg. 223, 342–347 (1996).

[26] Sheppard DG, Whitman GJ, Huynh PT et al. Tubular carcinoma of the breast: mammographic and sonographic features. Am. J. Roentgenol. 174, 253–257 (2000).

[27] Valtola, Reija, et al. "VEGFR-3 and its ligand VEGF-C are associated with angiogenesis in breast cancer." The American journal of pathology 154.5 (1999): 1381-1390.

[28] Kaipainen A, Korhonen J, Mustonen T, van Hinsbergh VM, Fang G-H, Dumont D, Breitman M, Alitalo K: Expression of the fms-like tyrosine kinase FLT4 gene becomes restricted to endothelium of lymphatic vessels during development. Proc Natl Acad Sci USA 1995, 92:3566–3570

[29] Mitrani, Alex. "Evaluating Categorical Models II: Sensitivity and Specificity." Medium, Towards Data Science, 6 Dec. 2019, towardsdatascience.com/evaluating-categorical-models-ii-sensitivity-and-specificity-e181e573cff8.

[30] "Digital Mammography - Mammography - Imaginis - The Women's Health & Wellness Resource Network". www.imaginis.com. Archived from the original on 30 January 2012. Retrieved 4 May 2018.

[31] Breast Cancer: Screening". United States Preventive Services Task Force. Archived from the original on 2016-01-15

[32] "Mammography-leaflet; Screening for breast cancer with mammography" (PDF). Archived (PDF) from the original on 2012-09-05. Retrieved 2012-06-24.

[33] Dhawan, Atam P. (2003). Medical Image Analysis. Hoboken, NJ: Wiley-Interscience. ISBN 978-0-471-45131-0

[34] "Breast ultrasound: MedlinePlus Medical Encyclopedia". Retrieved 2010-08-22

[35] Lindner J.R. (2004). "Microbubbles in medical imaging: current applications and future directions". Nat Rev Drug Discov. 3 (6): 527–32. doi:10.1038/nrd1417. PMID 15173842

[36] Sidhu, Paul; Cantisani, Vito; Deganello, Annamaria; Dietrich, Christoph; Duran, Carmina; Franke, Doris; Harkanyi, Zoltan; Kosiak, Wojciech; Miele, Vittorio; Ntoulia, Aikaterini; Piskunowicz, Maciej; Sellars, Maria; Gilja, Odd (2016). "Role of Contrast-Enhanced Ultrasound (CEUS) in Paediatric Practice: An EFSUMB Position Statement".

Ultraschall in der Medizin – European Journal of Ultrasound. 38 (1): 33–43. doi:10.1055/s-0042-110394. ISSN 0172-4614. PMID 27414980.

[37] McRobbie DW, Moore EA, Graves MJ, Prince MR (2007). MRI from Picture to Proton. Cambridge University Press. p. 1. ISBN 978-1-139-45719-4.

[38] Jones J, Gaillard F. "MRI sequences (overview)". Radiopaedia. Retrieved 2017-10-15.

[39] Goscin, Christopher P.; Berman, Claudia G.; Clark, Robert A. (2001). "Magnetic Resonance Imaging of the Breast". Cancer Control. 8 (5): 399–406. doi:10.1177/107327480100800502. PMID 11579335.

[40] Herman, G. T., Fundamentals of computerized tomography: Image reconstruction from projection, 2nd edition, Springer, 2009

[41] Žabić S, Wang Q, Morton T, Brown KM (March 2013). "A low dose simulation tool for CT systems with energy integrating detectors". Medical Physics. 40 (3): 031102. Bibcode:2013MedPh..40c1102Z. doi:10.1118/1.4789628. PMID 23464282.

[42] Niklason, Loren, "Breast tomosynthesis-an overview" 2018

[43] Dobbins JT, 3rd; Godfrey, DJ (7 October 2003). "Digital x-ray tomosynthesis: current state of the art and clinical potential". Physics in Medicine and Biology. 48 (19): R65–106. doi:10.1088/0031-9155/48/19/r01. PMID 14579853.

[44] Sechopoulos, Ioannis (2013). "A review of breast tomosynthesis. Part II. Image reconstruction, processing and analysis, and advanced applications". Medical Physics. 40 (1): 014302. doi:10.1118/1.4770281. PMC 3548896. PMID 23298127.

[45] Teertstra HJ, Loo CE, van den Bosch MA et al (2009) Breast tomosynthesis in clinical practice: initial results. Eur Radiol 20:16–24

[46] Skaane P, Gullien R, Bjorndal H et al (2012) Digital breast tomosynthesis (DBT): initial experience in a clinical setting. ActaRadiol 53:524–529

[47] Lång, K; Andersson, I; Zackrisson, S (2014). "Breast cancer detection in digital breast tomosynthesis and digital mammography—a side-by-side review of discrepant cases". The British Journal of Radiology. 87 (1040): 20140080. doi:10.1259/bjr.20140080. ISSN 0007-1285. PMC 4112403. PMID 24896197.

[48] Michell, M. J., and B. Batohi. "Role of tomosynthesis in breast imaging going forward." Clinical radiology 73.4 (2018): 358-371.

[49] Vedantham S, Karellas A, Vijayaraghavan GR, et al. Digital breast tomosynthesis: state of the art. Radiology 2015;277(3):663e84.

[50] Michell MJ, Iqbal A, Wasan RK, et al. A comparison of the accuracy of film-screen mammography, full-field digital mammography and digital breast tomosynthesis. Clin Radiol 2012;67:976e81.

[51] Chae EY, Kin HH, Cha JH, et al. Detection and characterization of breast lesions in a selective diagnostic population: diagnostic accuracy study for comparison between one-view digital breast tomosynthesis and two-view full-field digital mammography. Br J Radiol 2016;89:20150743, https://doi.org/10.1259/bjr.20150743.

[52] Waldherr C, Cerny P, Altermatt HJ, et al. Value of one-view breast tomosynthesis versus two-view mammography in diagnostic workup of women with clinical signs and symptoms and in women recalled
from screening. AJR Am J Roentgenol 2013;200:226e31.

[53] Wasan R, Morel J, Iqbal A. Digital breast tomosynthesis improves the accuracy of the diagnosis of circumscribed lesions because of increase of margin visibility. Breast Cancer Res 2014;16(Suppl. 1):O6. https://doi.org/10.1186/bcr3701.

[54] Chamming's F, Kao E, Aldis A, et al. Imaging features and conspicuity of invasive lobular carcinomas on digital breast tomosynthesis. Br J Radiol2017;90:20170128, https://doi.org/10.1259/bjr.20170128.

[55] Gilbert FJ, Tucker L, Gillian MG, et al. The TOMMY trial: a comparison of TOMosynthesis with digital mammographY in the UK NHS Breast Screening Programme d a multicenter retrospective reading study comparing the diagnostic performance of digital breast tomosynthesis and digital mammography with digital mammography alone. Health Technol Assess 2015;19(4):1e136. https://doi.org/10.3310/hta19040.

[56] Thibault, Fabienne, et al. "Digital breast tomosynthesis versus mammography and breast ultrasound: a multireader performance study." *European radiology* 23.9 (2013): 2441-2449.

[57] Narkhede, Sarang. "Understanding AUC - ROC Curve." *Medium*, Towards Data Science, 26 May 2019, towardsdatascience.com/understanding-auc-roc-curve-68b2303cc9c5.

[58] Svahn TM, Chakraborty DP, Ikeda D et al (2012) Breast tomosynthesis and digital mammography: a comparison of diagnostic accuracy. Br J Radiol 5:e1074–e1082

[59] Gennaro G, Hendrick RE, Di Maggio C et al (2012) Digital breast tomosynthesis: radiologists' learning process. RSNA, Chicago. Available via http://rsna2012.rsna.org/search/index.cfm. Accessed 9 January 2013

[60] Carr, D., Brown, J., Bydder, G., Steiner, R., Weinmann, H., Speck, U., . . . Young, I. (1984). Gadolinium-DTPA as a contrast agent in MRI: Initial clinical experience in 20 patients. American Journal of Roentgenology,143(2), 215-224. doi:10.2214/ajr.143.2.215

[61] Brasch, Robert C., et al. "Brain nuclear magnetic resonance imaging enhanced by a paramagnetic nitroxide contrast agent: preliminary report." American journal of roentgenology 141.5 (1983): 1019-1023.

[62] Gadolinium-based contrast agents for magnetic resonance cancer imaging (Zhuxian Zhou and Zheng-Rong Lu)

[63] Caschera, L., Lazzara, A., Piergallini, L., Ricci, D., Tuscano, B., & Vanzulli, A. (2016). Contrast agents in diagnostic imaging: Present and future. Pharmacological Research, 110, 65-75. doi:10.1016/j.phrs.2016.04.023

[64] Herman, Computed tomography contrast enhancement principles and the use of high-concentration contrast media, J. Comput. Assist. Tomogr. 28 (Suppl 1) (2004) S7–11

[65] A.L. Klibanov, Ligand-carrying gas-filled microbubbles: ultrasound contrast agents for targeted molecular imaging, Bioconjugate Chem. 16 (2005) 9–17.

[66] Dromain, C., Balleyguier, C., Muller, S., Mathieu, M., Rochard, F., Opolon, P., & Sigal, R. (2006). Evaluation of Tumor Angiogenesis of Breast Carcinoma Using Contrast-Enhanced Digital Mammography. American Journal of Roentgenology,187(5). doi:10.2214/ajr.05.1944

[67] 'X-ray-Computed Tomography Contrast Agents' Mattrey, R. F., Aguirre, D. A. *Academy of Radiology*, 2003, 10, 1450.

[68] Seltzer, S.E. et. al. *Am. J. Roentgenol*. 1984, *143*, 575.

[69] Werner, et al. "MCNP Version 6.2 Release Notes." *MCNP Version 6.2 Release Notes (Technical Report) | OSTI.GOV*, 5 Feb. 2018, www.osti.gov/biblio/1419730-mcnp-version-release-notes.

[70] Lemosquet, A., L. De Carlan, and I. Clairand. "Voxel anthropomorphic phantoms: review of models used for ionising radiation dosimetry." *Radioprotection* 38.4 (2003): 509-528.

[71] "The National Library of Medicine's Visible Human Project." *U.S. National Library of Medicine*, National Institutes of Health, www.nlm.nih.gov/research/visible/visible_human.html.

[72] Xu, X. G., T. C. Chao, and A. Bozkurt. "VIP-Man: an image-based whole-body adult male model constructed from color photographs of the Visible Human Project for multi-particle Monte Carlo calculations." *Health Physics* 78.5 (2000): 476-486.

[73] Aldridge, Jennifer S., Paul J. Reckwerdt, and Thomas Rockwell Mackie. "A proposal for a standard electronic anthropomorphic phantom for radiotherapy." *Medical physics* 26.9 (1999): 1901-1903.

[74] C.D. Werner, et. al. "Applications of the visible man dataset in electrocardiology: calculation and visualization of body surface potential maps of a complete heart cycle" in *Proc. Second Users Conference of the National Library of Medicine's Visible Human Project*, 1998.

[75] Anderson, Casey Alan, Karen C. Kelley, and John T. Goorley. *Mesh human phantoms with MCNP*. No. LA-UR-12-01307; LA-UR-12-1307. Los Alamos National Lab.(LANL), Los Alamos, NM (United States), 2012.

[76] Zhang, Rui, et al. "Advantages of MCNPX-based lattice tally over mesh tally in high-speed Monte Carlo dose reconstruction for proton radiotherapy." *Nuclear technology* 183.1 (2013): 101-106..

[77] Imaging of deep brain stimulation leads using extended Hounsfield unit CT. Stereotact Funct Neurosurg. 2009;87(3):155-60. doi: 10.1159/000209296

[78] Long, Daniel J et al. "Monte Carlo simulations of adult and pediatric computed tomography exams: validation studies of organ doses with physical phantoms." Medical physics vol. 40,1 (2013): 013901. doi:10.1118/1.4771934

[79] Cranley K., Gilmore B. J., Fogarty G. W. A., and Desponds L., "Catalogue of diagnostic x-ray spectra and other data," Report No. 78 (The Institute of Physics, London,1997). [Google Scholar] [Ref list]

[80] Organ doses for reference adult male and female undergoing computed tomography estimated by Monte Carlo simulations. Lee C, Kim KP, Long D, Fisher R, Tien C, Simon SL, Bouville A, Bolch WE Med Phys. 2011 Mar; 38(3):1196-206.

[81] Li X, Samei E, Segars WP, Sturgeon GM, Colsher JG, Toncheva G, Yoshizumi TT, Frush DP Med Phys. 2011 Jan; 38(1):397-407

[83] E. C. Snow "MCNP Radiography Patch" Los Alamos National Laboratory memorandum XTM:96-169(U), April 25, (1996)

[84] Manual, Abaqus Scripting User's. "Abaqus 6.11." *http://130.149* 89.2080 (2012): v6.

[85] Werner, Christopher J. "MCNP Users Manual-Code Version 6.2." *Los Alamos National Laboratory, Los Alamos* (2017).

[86] Strudley, C., P. Looney, and K. Young. "Technical evaluation of Hologic Selenia Dimensions digital breast tomosynthesis system (NHSBSP equipment report 1307 version 2)." *Sheffield: NHS Cancer Screening Programmes* (2014).

[87] D'angelo, Chelsea, Steven S. Mc Cready, and Karen C. Kelley. *Modeling radiation transport using MCNP6 and Abaqus/CAE*. No. LA-UR-12-01321; LA-UR-12-1321. Los Alamos National Lab. (LANL), Los Alamos, NM (United States), 2012.

[88] Martz, Roger L. "The MCNP6 Book On Unstructured Mesh Geometry: User's Guide." *LA-UR-11-05668 Rev. 8, MCNP6 code release to RSICC, Oak Ridge, TN and general distribution* (2014).

[89] Sechopoulos, Ioannis. "A review of breast tomosynthesis. Part I. The image acquisition process." Medical physics vol. 40,1 (2013): 014301. doi:10.1118/1.4770279

[90] Harns, David. "Correcting CT Scanner Artifacts: Streak Artifacts." *Medical Imaging Equipment Guide*, info.blockimaging.com/correcting-ct-scanner-artifacts-streak-artifacts.

[91] Clover Learning. "Anode Heel Effect (X-Ray Tube)." *YouTube*, 20 May, 2020. https://www.youtube.com/watch?v=M9S1ULdwav8

[92] Scratchapixel. *Introduction to Shading (Diffuse and Lambertian Shading)*, 15 Aug. 2014, www.scratchapixel.com/lessons/3d-basic-rendering/introduction-to-shading/diffuse-lambertian-shading.